

Alma Mater Studiorum Università di Bologna  
Archivio istituzionale della ricerca

The role of trapped fluids during the development and deformation of a carbonate/shale intra-wedge tectonic mélange (Mt. Massico, Southern Apennines, Italy)

This is the final peer-reviewed author's accepted manuscript (postprint) of the following publication:

*Published Version:*

Smeraglia L., Aldega L., Bernasconi S.M., Billi A., Boschi C., Caracausi A., et al. (2020). The role of trapped fluids during the development and deformation of a carbonate/shale intra-wedge tectonic mélange (Mt. Massico, Southern Apennines, Italy). JOURNAL OF STRUCTURAL GEOLOGY, 138, --- [10.1016/j.jsg.2020.104086].

*Availability:*

This version is available at: <https://hdl.handle.net/11585/770627> since: 2020-09-08

*Published:*

DOI: <http://doi.org/10.1016/j.jsg.2020.104086>

*Terms of use:*

Some rights reserved. The terms and conditions for the reuse of this version of the manuscript are specified in the publishing policy. For all terms of use and more information see the publisher's website.

This item was downloaded from IRIS Università di Bologna (<https://cris.unibo.it/>).  
When citing, please refer to the published version.

(Article begins on next page)

This is the final peer-reviewed accepted manuscript of:

Smeraglia L.; Aldega L.; Bernasconi S.M.; Billi A.; Boschi C.; Caracausi A.; Carminati E.; Franchini S.; Rizzo A.L.; Rossetti F.; Vignaroli G.: *The role of trapped fluids during the development and deformation of a carbonate/shale intra-wedge tectonic mélange (Mt. Massico, Southern Apennines, Italy)*

JOURNAL OF STRUCTURAL GEOLOGY

VOL. 138

ISSN 0191-8141

DOI: 10.1016/j.jsg.2020.104086

The final published version is available online at:

<https://dx.doi.org/10.1016/j.jsg.2020.104086>

Terms of use:

Some rights reserved. The terms and conditions for the reuse of this version of the manuscript are specified in the publishing policy. For all terms of use and more information see the publisher's website.

This item was downloaded from IRIS Università di Bologna (<https://cris.unibo.it/>)

**When citing, please refer to the published version.**

# **The role of trapped fluids during the development and deformation of a carbonate/shale intra-wedge tectonic mélange**

Luca Smeraglia<sup>1,2,3\*</sup>, Luca Aldega<sup>4</sup>, Stefano Bernasconi<sup>5</sup> Andrea Billi<sup>1</sup>, Chiara Boschi<sup>6</sup>, Antonio Caracausi<sup>7</sup>, Eugenio Carminati<sup>1,4</sup>, Stefania Franchini<sup>1,4</sup>, Andrea Luca Rizzo<sup>7</sup>, Federico Rossetti<sup>8</sup>, Gianluca Vignaroli<sup>9</sup>

1. Consiglio Nazionale delle Ricerche, IGAG, c.o. Dipartimento di Scienze della Terra, Sapienza Università di Roma, P.le Aldo Moro 5, 00185 Roma, Italy

2. formerly at Dipartimento di Scienze della Terra, Sapienza Università di Roma, P.le Aldo Moro 5, 00185, Roma, Italy

3. formerly at Chrono-Environnement, Université de Bourgogne Franche-Comté, 16 Route de Gray, 25000 Besançon, France.

4. Dipartimento di Scienze della Terra, Sapienza Università di Roma, P.le Aldo Moro 5, 00185, Roma, Italy

5. Geological Institute, ETH Zürich, Sonneggstrasse 5, 8092 Zürich, Switzerland

6. Istituto di Geoscienze e Georisorse, Consiglio Nazionale delle Ricerche, Via Moruzzi 1, 56124 Pisa, Italy

7. Istituto Nazionale di Geofisica e Vulcanologia, Sezione di Palermo, Via Ugo La Malfa 153, 90146 Palermo, Italy

8. Dipartimento di Scienze, Università Roma Tre, Largo San Leonardo Murialdo, 1, 00146, Roma, Italy

9. Dipartimento di Scienze Biologiche, Geologiche e Ambientali, BiGeA, Università di Bologna, 40126 Bologna, Italy

Luca Smeraglia: [luca.smeraglia@cnr.it](mailto:luca.smeraglia@cnr.it)

Luca Aldega: [luca.aldega@uniroma1.it](mailto:luca.aldega@uniroma1.it)

Stefano Bernasconi: [stefano.bernasconi@erdw.ethz.ch](mailto:stefano.bernasconi@erdw.ethz.ch)

Andrea Billi: [andrea.billi@cnr.it](mailto:andrea.billi@cnr.it)

Chiara Boschi: [chiara.boschi@igg.cnr.it](mailto:chiara.boschi@igg.cnr.it)

Antonio Caracausi: [antonio.caracausi@ingv.it](mailto:antonio.caracausi@ingv.it)

Eugenio Carminati: [eugenio.carminati@uniroma1.it](mailto:eugenio.carminati@uniroma1.it)

Stefania Fanchini: [stefania.franchini@uniroma1.it](mailto:stefania.franchini@uniroma1.it)

28    Andrea Luca Rizzo: [andrea.rizzo@ingv.it](mailto:andrea.rizzo@ingv.it)

29    Federico Rossetti: [federico.rossetti@uniroma3.it](mailto:federico.rossetti@uniroma3.it)

30    Gianluca Vignaroli: [gianluca.vignaroli@unibo.it](mailto:gianluca.vignaroli@unibo.it)

31

32    \*Corresponding author: Dipartimento di Scienze della Terra, Sapienza Università di Roma, Piazzale Aldo

33    Moro 5, 00185 Roma, Italy. Phone +39 06 49914156

34    E-mail address: [luca.smeraglia@cnr.it](mailto:luca.smeraglia@cnr.it) (Luca Smeraglia)

35

36

37

38

39

40

41

42

43

44

45

46

47

48

49

50

51

52

53

**Abstract:** In contrast to the numerous studies on exhumed tectonic mélanges along subduction channels, in accretionary wedge interiors, deformation mechanisms and related fluid circulation in tectonic mélanges are still underexplored. Here we combine structural and microstructural observations with geochemical (stable and clumped isotopes and isotope composition of noble gases in fluid inclusions of calcite veins) and geochronological data (U-Pb dating) to define deformation mechanisms and syn-tectonic fluid circulation within the Mt. Massico intra-wedge tectonic mélange, located in the inner part of the central-southern Apennines accretionary wedge, Italy. This mélange developed at the base of a clastic succession, and shear deformation was characterized by disruption of the primary bedding, mixing, and deformation of relicts of competent olistoliths and strata within a weak matrix of deformed clayey and marly interbeds. Recurrent cycles of mutually overprinting fracturing/veining and pressure-solution processes generated a block-in-matrix texture. The geochemical signatures of syn-tectonic calcite veins suggest calcite precipitation in a closed system from warm (108-147 °C) paleofluids, with  $\delta^{18}\text{O}$  composition between +9‰ and 14‰, such as trapped pore water from diagenesis after extensive  $^{18}\text{O}$  exchange with the local limestone host rock ( $\delta^{18}\text{O}$  values between +26‰ and +30‰) and/or derived by clay dehydration processes (at  $T > 120$  °C). The  $^3\text{He}/^4\text{He}$  ratios in fluid inclusions trapped in calcite veins are lower than 0.1 Ra, hence He was exclusively sourced from the crust, excluding mantle-derived fluids. We conclude that: (1) intraformational rheological contrasts, inherited trapped fluids, and low-permeability barriers such as clay-rich stylolites, can favour the development of fluid overpressure and the generation of intra-wedge tectonic mélanges; (2) clay-rich intra-wedge tectonic mélanges may generate efficient barriers within accretionary wedges for vertical and lateral redistribution of fluids from reservoirs outside the mélange. We highlight that the integration of geochemical and geochronological methods can be a powerful approach to better constrain, in the future, the burial-thermal evolution of fold and thrust belts and sedimentary basins.

79 **Keywords:** tectonic mélange; fault-fluid interaction; stable and clumped isotopes; carbonates and  
80 shales; fold and thrust belt

81

## 82 **1. Introduction**

83 Décollements and thrust faults are major structures that control the internal architecture of  
84 fold-and-thrust belts (e.g. Morley et al., 2017). In particular, décollements commonly generate  
85 along evaporite- or clay-rich formations, control the style and timing of folding and tectonic  
86 imbrication, and may act as barriers or conduits for crustal flow of fluids, including hydrocarbons.  
87 Décollements can often act as channelized paths for fluid redistribution within the crust (e.g.  
88 Vrolijk et al., 1988; Vannucchi et al., 2008).

89 The shearing of clay-rich and initially layered formations along décollements can generate  
90 tectonic mélanges through primary bedding disruption, pressure-solution, veining, and  
91 offscraping/mixing of blocks from competent formations located above and below the décollement  
92 horizon (see Festa et al., 2012 for review). Such deformations can lead to block-in-matrix fabrics,  
93 consisting of competent blocks scattered in a weak matrix, which are typically characterized by  
94 heterogeneous mechanical and permeability properties (e.g. Fagereng, 2011). Outcrop,  
95 microstructural, and geochemical characterizations of tectonic mélanges can contribute to constrain  
96 their spatio-temporal evolution as well as the mechanical properties and hydrogeological  
97 characteristics (paleofluid flow).

98 In this context, several studies focused on tectonic mélanges exhumed from basal  
99 décollements at the subduction interface along the toe of accretionary wedges and from subduction  
100 channels (e.g. Meneghini et al., 2009; Vannucchi et al., 2008; see Festa et al., 2012 for review),  
101 where deformation can reach metamorphic conditions (e.g. Fagereng and Cooper, 2010). Only few  
102 studies focused on intra-wedge tectonic mélanges developed at diagenetic P-T conditions along  
103 décollements at the base of thrust sheets (e.g. Vannucchi and Bettelli, 2002; Codegone et al., 2012;  
104 Dewever et al., 2013; Ogata et al., 2012; Smeraglia et al., 2019). However, intra-wedge tectonic

105 mélanges may strongly affect the mechanical behavior of inner décollements, thus influencing  
106 accretionary wedge geometry and kinematics, and can modulate the transport of fluids (i.e. water,  
107 hydrocarbon) across fold-and-thrust belts. Therefore, the understanding of mechanical and  
108 hydrological properties of exhumed mélanges is fundamental to unravel fluid (paleo)pathways and  
109 assess potential reservoirs for geofluid (i.e. hydrocarbon) accumulation in fold-and-thrust belts.

110 For these reasons, here we combine outcrop and microstructural observations with  
111 geochemical analyses (stable and clumped isotopes and isotope composition of noble gases in fluid  
112 inclusions of calcite veins) to unravel the deformation mechanisms, paleohydrology (i.e., fluid  
113 conduit/barrier behavior), and the temperature conditions during fluid flow within a 150 m-thick  
114 intra-wedge tectonic mélange in the Mt. Massico Ridge (e.g. Billi et al., 1997; Vitale et al., 2018;  
115 Smeraglia et al., 2019), which is located in the inner sector (Tyrrhenian side) of the central-southern  
116 Apennines fold-and-thrust belt. In this area, outcrop conditions allowed the reconstruction of syn-  
117 tectonic paleofluid circulation and the unraveling of progressive intra-wedge mélange deformation,  
118 from the undeformed host rock to the finite fabric development by tectonic deformation.

119

## 120 **2. Geological background**

### 121 *2.1 Central-southern Apennines*

122 The central-southern Apennines are a late Oligocene to present fold-and-thrust belt generated  
123 by the eastward rollback of the west-dipping subduction of the Adriatic plate below the European  
124 continental margin (Fig. 1a; e.g., Carminati et al., 2012). Orogenic accretion was accomplished  
125 through and accommodated by a set of NE-verging thrust systems, which scraped off pre- and syn-  
126 orogenic deposits of the Adriatic plate (Fig. 1b). The pre-orogenic deposits consist of ~4,000-5,000  
127 m-thick Upper Triassic-Middle Miocene carbonate platform deposits (i.e. Apennine platform; e.g.  
128 Vezzani et al., 2010; Vitale and Ciarcia, 2018) and of ~100 m-thick middle Miocene hemipelagic  
129 marls deposited in a transitional foreland-to-foredeep environment (e.g., Vezzani et al., 2010). The  
130 syn-orogenic deposits consist of up to ~3,100 m-thick upper Miocene siliciclastic sandstones, marls,

131 and claystones deposited in a foredeep environment (e.g., Vitale and Ciarcia, 2018). Thrust faults  
132 developed during wedge accretion and juxtaposed pre-orogenic deposits onto syn-orogenic  
133 sediments, generating stacks of imbricate thrust sheets from the surface down to depths of ~10 km  
134 (Fig. 1a,b; e.g. Mostardini and Merlini, 1986; Vezzani et al., 2010). Since early Pliocene time, the  
135 internal and axial part of the central-southern Apennines belt underwent tectonic uplift and regional  
136 extension, related to the opening of the Tyrrhenian backarc basin and accommodated by the  
137 development of NW-SE-oriented extensional faults (Fig. 1a,b; Malinverno and Ryan, 1986).

138

## 139 2.2 The Mt. Massico ridge

140 Mt. Massico is a NNE-SSW-trending ridge located in the innermost part of the central-  
141 southern Apennines (Fig. 1a; e.g. Billi et al., 1997; Luiso et al., 2018; Vitale et al., 2018). It is  
142 bounded by NE-striking active extensional faults and surrounded by the Quaternary Garigliano and  
143 Volturno river plains, the Roccamonfina volcano (Quaternary), and the Tyrrhenian Sea basin (Figs.  
144 1a and 2a).

145 In the central and northeastern parts of the Mt. Massico ridge, Upper Triassic to Upper  
146 Cretaceous carbonates are exposed (Fig. 1a; Vitale et al., 2018) and arranged to form a ENE-  
147 verging asymmetric anticline with an upright forelimb and a WSW-dipping (40°-50°) backlimb  
148 (Fig. 1a). In the forelimb, a thrust juxtaposes Upper Cretaceous limestones onto Tortonian syn-  
149 orogenic sandstones (see Figure 2 in Sgroso, 1974). The WSW-dipping backlimb continues in the  
150 southwestern part of the ridge, where middle-upper Miocene sediments are exposed (Fig. 2a,b).

151 This succession lies paraconformably atop Upper Cretaceous limestones and begins from the  
152 bottom with ~50 m-thick bryozoan-rich limestones of the Cusano Fm., followed upward by  
153 hemipelagic marls of the Longano Fm., with a preserved thickness of less than 1-3 meters (Sgroso,  
154 1974; Vitale et al., 2018) (Fig. 2a). Both these formations were deposited in a foreland environment  
155 and are Serravallian in age (Sgroso, 1974). Above the hemipelagic marls, the sedimentary  
156 succession evolves into the Tortonian-lower Messinian siliciclastic/carbonaticlastic deposits of the



157 Caiazzo Fm. (hereafter called clastic deposits, Fig. 2a,b), which are interpreted as wedge-top basin  
158 deposits (Vitale et al., 2018). The clastic deposits are made up of: (1) massive-to-bedded  
159 siliciclastic sandstones with clayey, marly, and calcarenite interbeds and (2) polymictic  
160 breccias/conglomerates characterized by Mesozoic-Cenozoic carbonate blocks and siliciclastic  
161 clasts (up to a few dm<sup>3</sup> in volume), including also clasts of volcanic, intrusive, and metamorphic  
162 rocks (Fig. 2a) (Sgrosso, 1974). The clastic deposits are unconformably overlain by well-bedded  
163 lower Messinian calcarenites (Fig. 2a). Intercalated within the clastic deposits are hundreds of  
164 olistoliths, from a few dm<sup>3</sup> to several thousands of m<sup>3</sup> in volume. Olistoliths consist of Mesozoic-  
165 Cenozoic limestones and exotic rocks not exposed in the local sedimentary succession (hereafter  
166 named exotic olistoliths), such as marbles and recrystallized carbonates as well as volcanic,  
167 intrusive, and metamorphic rocks, and deep basinal Paleocene limestone blocks (Sgrosso, 1974; Di  
168 Girolamo et al., 2000; Vitale et al., 2018). The total thickness of the upper Tortonian-lower  
169 Messinian succession is ~800 m (Smeraglia et al., 2019).

170

### 171 2.3 The Mt. Massico *mélange*

172 The about ~150 m thick basal portion of the clastic deposits and the underlying hemipelagic  
173 marls are strongly deformed, showing a block-in-matrix fabric typical of tectonic *mélanges* (Fig.  
174 2a,b; Vitale et al., 2018; Smeraglia et al., 2019). Based on new geological mapping (see also Vitale  
175 et al., 2018 for new stratigraphic constraints), structural analysis, U-Pb dating (syn-tectonic calcite  
176 ages of  $10.5 \pm 2.5$  My,  $7.0 \pm 1.6$  My, and  $5.1 \pm 3.7$ ), and thermal modelling constrained by mixed  
177 layers illite-smectite, Smeraglia et al. 2019 proposed that the Mt. Massico tectonic *mélange*  
178 developed, since late Messinian times, by out-of sequence thrusting of multiple thrust sheets above  
179 the clastic deposits located in the backlimb of the Mt. Massico anticline (Fig. 9a-c) and by  
180 localization of deformation at the base of clastic deposits. In this context, the original stratigraphic  
181 boundary between the clastic deposits/hemipelagic marls deposits and the underlying limestones  
182 was sheared as a *décollement* horizon and an intra-wedge tectonic *mélange* developed due to the

183 strong rheological contrast between the weak clastic deposits and the competent limestones. This  
184 mélange is characterized by a pervasive S-C and S-CC' fabrics showing a coherent transport  
185 direction towards ESE, accommodated by partitioned reverse and dextral transpressive tectonics  
186 (Fig. 2a; Smeraglia et al., 2019).

187

### 188 **3. Methods**

189 Aiming at characterize the structurally-controlled fluid circulation and the geochemical  
190 signature of the syn-tectonic fluids in the transition from the undeformed host rock to the tectonic  
191 mélange formation, we focused our structural and geochemical studies within the San Sebastiano  
192 and Mt. Cicoli areas (Fig. 2). In these areas, it is in fact possible to observe the progressive  
193 transition from poorly deformed clastic deposits to moderately and strongly deformed parts of the  
194 tectonic mélange along the boundary with the underlying bryozoan-rich limestones of the Cusano  
195 Fm. (Fig. 2a). To achieve this purpose we integrated: (1) geological field mapping at 1:10,000  
196 scale, and available maps (Billi et al., 1997; Vitale et al., 2018; Smeraglia et al., 2019), to unravel  
197 the structural architecture and the deformation history of the intra-wedge tectonic mélange; (2)  
198 microstructural (optical microscope) analyses to unravel the deformation mechanisms acting during  
199 mélange generation; (3) Stable carbon and oxygen and carbonate clumped isotopes to reconstruct  
200 the origin and precipitation temperatures of the paleofluid circulating during mélange generation;  
201 (4) H<sub>2</sub>O+CO<sub>2</sub>, N<sub>2</sub>, and minor gaseous species (He, Ne, and Ar concentrations and isotope ratios) in  
202 fluid inclusions on previously U-Pb dated syn-tectonic carbonate samples/veins (ages of  $10.5 \pm 2.5$   
203 My,  $7.0 \pm 1.6$  My, and  $5.1 \pm 3.7$ ; Smeraglia et al., 2019) . Sample preparation and analytical details  
204 are described in the Supplementary Material.

205

### 206 **4. Results**

#### 207 *4.1 Outcrop observations*

208 A progressive transition in shear strain localization is observed when moving across strike  
209 along the studied area. Within the poorly deformed clastic deposits, bedding is still observable (Fig.  
210 3a,b). The competent sandstones beds and the marly-shaly interbeds are gently folded and/or cut by  
211 low-displacement reverse faults displaying a ramp-and-flat geometry, with the flat segment located  
212 within marly and shaly interbeds (Fig. 3b). The marly and shaly interbeds are characterized by a  
213 weak and bedding-parallel scaly foliation (Fig. 3a,b); however, in places, an incipient S-C fabric  
214 characterized by bedding-parallel S planes and bedding-oblique C planes occurs dismembering the  
215 sandstone interbeds (Fig. 3a).

216 We recognized a up ~100 m-thick zone, referred as moderately deformed zone of the tectonic  
217 *mélange*, exposed within a diffuse boundary between the poorly deformed clastic deposits and the  
218 strongly deformed part of the tectonic *mélange* (Fig. 2). This zone is characterized by still  
219 detectable primary structures such as bedding, but competent strata (i.e. sandstones and calcarenites  
220 interbeds) show pinch-and-swell and boudin-like geometries. Pervasive and anastomosing bedding-  
221 parallel scaly foliation occurs within marly and shaly interbeds (Fig. 3c,d) and, in places, S-C  
222 fabrics can be observed (Fig. 3e). With increasing deformation, primary foliation is dismembered  
223 and relicts of bedding are scattered within the scaly foliation generating a block-in-matrix fabric  
224 (Fig. 3d-e). In particular, such relicts show bedding-perpendicular calcite veins (Fig. 3d,e).

225 The strongly deformed part of the tectonic *mélange*, up to ~50 m-thick, shows well-developed  
226 S-C and S-CC' tectonites and sedimentary structures are completely obliterated by tectonic fabric  
227 (Figs. 3f-h and 4a,b). In particular, the WNW- to WSW-dipping S- and C-surfaces show dip angles  
228 ranging ~60°-70° and ~10°-30°, respectively, with kinematic indicators showing mainly reverse  
229 dip-slip to right-lateral transpressional movements (Fig. 2a). Marls and shales are affected by S-C  
230 foliations and clasts of competent rocks (i.e. sandstones and calcarenites) are deformed in  
231 sigmoidal-lozenge-shaped structures consistent with the overall sense of shear (Figs. 3f-g and 4a-c).  
232 Stylolites and slickenfibers are aligned parallel respect to S and C planes, respectively, whereas  
233 sigmoidal clasts of competent rocks are permeated by calcite veins (Figs. 3g,h and 4d).

234 With increasing deformation, the sigmoidal relicts of sedimentary structures are progressively  
235 thinned and completely obliterated by S-C foliation so that it is difficult to distinguish them from  
236 the pervasive scaly foliation at the naked eye (Fig. 4c). In places, foliated marls and shales wrap  
237 olistoliths inherited from clastic deposits. The olistoliths preserve their original (from irregular to  
238 rounded) shapes, generating a block-in-matrix fabric (Fig. 4e-g). Convolute/contorted foliations  
239 also occur (Fig. 4h). Their origin is not clear and it cannot be excluded that they may be relicts of  
240 soft sediment (fluid escape) structures. When observable, the boundary between the tectonic  
241 mélange and the underlying bryozoan-rich limestones (not affected by deformation and with  
242 sedimentary structures and fossils still recognizable) is sharp.

243

#### 244 *4.2 Microstructural observations*

245 We focused our microstructural observations on the strongly deformed parts of the tectonic  
246 mélange, with special focus on the sigmoidal-lozenge clasts of competent rocks (i.e. sandstones and  
247 calcarenites), since they are cohesive and can be easily cut for thin section preparation.

248 The sigmoidal-lozenge clasts are characterized by pervasive stylolites, parallel to S, C, and C'  
249 planes (Fig. 5a-c). Stylolites evolve from rough, teeth-shaped, and indented morphology (Figs. 5a-c  
250 and 6a-b) to smooth, continuous, and thick (up to 1 mm) dissolution seams (Figs. 5a-c and 6c) filled  
251 by insoluble material (i.e. clay minerals and oxides), small clasts of host rock limestones, and  
252 fragments of calcite veins (Fig. 6c). Stylolites and dissolution seams bound sigmoids defining a  
253 fabric sub-parallel to S, C, and C' planes (Figs. 5a-c and 6a,b). Sigmoids consist of host rock  
254 commonly with deformed microfossils, and/or reworked calcite veins (Fig. 6a,b).

255 We identify fibrous and blocky calcite veins. Fibrous veins are oriented perpendicular to  
256 stylolites and are characterized by fibrous crystals perpendicular to vein margins (Fig. 6 d-f).  
257 Crystals are deformed by stylolites (Figs. 6d-f and 7a). The slickenfibers observed at the outcrop  
258 scale along S, C, and C' planes are characterized, at the microscale, by fibrous veins located along  
259 stylolite jogs, characterized by fibrous crystals parallel to stylolites (Fig. 6b,f). In places, fibrous

260 veins occur within thick dissolution seams (Fig. 7a,b). In this case, vein margins and fibrous  
261 crystals are roughly parallel and perpendicular to dissolution seam margins, respectively (Fig. 7a,b).  
262 Blocky veins are filled by blocky to elongated-blocky calcite crystals and are oriented parallel,  
263 perpendicular, or oblique to stylolites (Fig. 7c,d).

264 Concerning the relative timing of structures, we observed mutual crosscutting relationships  
265 between veins and stylolites (Figs. 5c and 7f). In particular, blocky veins perpendicular to stylolites  
266 cut or are deformed by stylolites and/or by blocky/fibrous veins oriented oblique to stylolites (Figs.  
267 5 and 7c-f). Fibrous veins parallel and/or perpendicular to stylolites are deformed by stylolites  
268 and/or by blocky veins oriented oblique to stylolites (Figs. 5, 7a,b, and 6d-f)

269

#### 270 *4.3 Stable and clumped isotopes*

271 Results from stable and clumped isotopes analyses are shown in Fig. 8 and listed in Table S1  
272 and S2. Results are reported in the conventional  $\delta$  notation with respect to the Vienna Pee Dee  
273 Belemnite (VPDB) for  $\delta^{13}\text{C}$  and Vienna Standard Mean Ocean Water (VSMOW) for  
274 Clumped isotopes are reported in the Carbon Dioxide Equilibrium Scale (Dennis et al. 2011).

275 The host rock  $\delta^{13}\text{C}$  and  $\delta^{18}\text{O}$  values, measured on limestones interbeds within clastic deposits,  
276 range between -0.5‰ and +1.5‰, and between +26‰ and +29.5‰, respectively. Such values are  
277 typical of Miocene marine carbonates in the Apennines, Italy (e.g., Hilgen et al., 2005).

278 Blocky veins  $\delta^{13}\text{C}$  and  $\delta^{18}\text{O}$  values range between 0‰ and +0.8‰ and between +22.3‰ and  
279 +27‰, respectively, with one blocky vein showing  $\delta^{13}\text{C}$  and  $\delta^{18}\text{O}$  values overlapping those of the  
280 host rock. Fibrous veins  $\delta^{13}\text{C}$  and  $\delta^{18}\text{O}$  values range between -0.4‰ and +1.6‰ and between  
281 +22.4‰ and +27.8‰, respectively. Three fibrous veins show  $\delta^{13}\text{C}$  and  $\delta^{18}\text{O}$  values overlapping  
282 those of the host rock. Overall, both blocky and fibrous veins show  $\delta^{13}\text{C}$  values overlapping with  
283 those of the host rock and an average  $\delta^{18}\text{O}$  depletion of ~4‰ respect to the host rock.

284 Clumped-isotope data from blocky veins (four samples) and fibrous veins (five samples)  
285 yields  $\Delta 47$  values between 0.424 and 0.482 (Table S2). These values correspond to temperatures

286 between  $108 \pm 13$  °C and  $147 \pm 20$  °C (Fig. 8b and Table S1), using the equation of Bernasconi et  
287 al. (2018). The calculated  $\delta^{18}\text{O}$  paleofluid compositions, using the O'Neil et al. (1969) equation  
288 developed for calcite precipitation temperature in the 0-500 °C range, range between 9.1‰ and  
289 13.7‰ (Fig. 8b and Table S1).

290

#### 291 *4.4 Noble gas analysis*

292 The concentrations of  $\text{CO}_2+\text{H}_2\text{O}$ ,  $\text{N}_2$ , light noble gases (He, Ne, Ar), and  $^3\text{He}/^4\text{He}$ ,  $^4\text{He}/^{20}\text{Ne}$ ,  
293  $^{40}\text{Ar}/^{36}\text{Ar}$  isotopic ratios in fluid inclusions hosted in syntectonic calcite veins (samples 239, 257  
294 and 260) are reported in Table S3.

295  $\text{CO}_2+\text{H}_2\text{O}$  and  $\text{N}_2$  show concentrations ranging between  $1.1 \times 10^{-6}$  and  $8.3 \times 10^{-6}$  mol/g and  
296 between  $3.1 \times 10^{-7}$  and  $6.7 \times 10^{-7}$  mol/g, respectively. The  $\text{N}_2/\text{Ar}$  ratios range between 3092 and 3633.  
297 These values are much more higher than the  $\text{N}_2/\text{Ar}$  ratio in the atmosphere (84.1) and the  $\text{N}_2/\text{Ar}$   
298 ratio in air-saturated water at standard temperature and pressure (38). The  $^{40}\text{Ar}/^{36}\text{Ar}$  ratios vary from  
299 367.3 to 389.9, slightly higher than the  $^{40}\text{Ar}/^{36}\text{Ar}$  ratio in atmosphere (298.6).

300 He/Ar and He/ $\text{N}_2$  ratios range between 0.06-0.14 and  $2.1\text{-}3.8 \times 10^{-5}$ , respectively, and are 1-2  
301 orders of magnitude higher than the theoretical values in the atmosphere and in the air-saturated  
302 water. The  $^4\text{He}/^{20}\text{Ne}$  ratios range between 51.7 and 96.5 and are more than two orders of magnitude  
303 higher than the typical  $^4\text{He}/^{20}\text{Ne}$  ratio in air saturated water (0.268), consistently with fluids trapped  
304 at great depth. All these ratios testify an excess of He and  $\text{N}_2$  respect to the typical concentrations in  
305 atmosphere-derived fluids. The  $^3\text{He}/^4\text{He}$  ratios, corrected for the air contamination (R/Ra ratio)  
306 range between 0.05 and 0.09, consistently with those of crustal fluids, thus excluding a contribution  
307 of He derived from atmospheric air and  $^3\text{He}$  from the mantle (Fig. 8d).

308 The  $^3\text{He}/^4\text{He}$  and  $^{40}\text{Ar}/^{36}\text{Ar}$  ratios are useful tracers to ascertain the origin of the fluids  
309 producing the mineralization. However, one condition is that these materials must contain volatiles  
310 trapped during precipitation processes and that their isotopic compositions have not been modified  
311 over time. Significant post precipitation processes that may affect the noble gases content in the

312 fluid inclusions regard the addition of (1)  $^4\text{He}$ ,  $^{40}\text{Ar}$  produced from the radiogenic decay of U, Th  
313 and K, and (2) cosmogenic  $^3\text{He}$  derived from the exposure to cosmic ray.

314 In order to estimate the contribution of radiogenic  $^{40}\text{Ar}$  into the fluid inclusions, we computed  
315 the  $^{40}\text{Ar}^*$ , which is the amount of  $^{40}\text{Ar}$  corrected for the atmospheric contributions ( $^{40}\text{Ar}^* =$   
316  $^{40}\text{Ar}/^{36}\text{Ar}_{\text{Measured}} - ^{40}\text{Ar}/^{36}\text{Ar}_{\text{Atmosphere}} \times ^{36}\text{Ar}_{\text{Measured}}$ ). The amounts of  $^{40}\text{Ar}^*$  range between  $8.99 \times 10^{-11}$   
317 to  $1.38 \times 10^{-10}$  mol/g (Table S3). The amounts of the measured  $^4\text{He}$  and measured  $^{40}\text{Ar}^*$  do not  
318 show any correlations with the ages of the veins (Fig. S1a,b), thus excluding the accumulation of  
319 radiogenic He and Ar produced in the veins by the U, Th and K decay during time.

320 All calcite veins have been collected in outcrops whose time of exposure to the cosmic ray at  
321 the surface is not evaluable; hence, the potential contribution of cosmogenic  $^3\text{He}$  trapped in the fluid  
322 inclusions is difficult to be assessed. However, there is no correlation between the amount of  $^3\text{He}$   
323 and the ages of calcite veins (Fig. S1c), which can supports a progressive accumulation over time of  
324 cosmogenic  $^3\text{He}$  and subsequent migration into the fluid inclusions.

325 On the basis of the average U and Th amounts in the veins of calcite (1.58 and 2.28 ppm for  
326 sample 257; 0.35 and 0.01 ppm for sample 239; 0.17 and 0.02 ppm for sample 260; Table S4) is  
327 possible to compute the potential  $^4\text{He}/^{40}\text{Ar}^*$  ratio produced by the decay of U and Th. The  
328 computed  $^4\text{He}/^{40}\text{Ar}^*$  ratios range between 10 and 100. These values are much higher than the same  
329 ratios in the fluid inclusions (0.61, 0.35, and 0.40 for samples 257, 239, and 260, respectively, Table  
330 S3). This suggests that the fluid inclusions are not modified by the contributions of both of  
331 radiogenic  $^4\text{He}$  and  $^{40}\text{Ar}$  produced within the rocks. We conclude that the isotopic ratios of He and  
332 Ar in the fluid inclusions are representative of the pristine isotopic signatures of the trapped fluids.

333

## 334 **5. Discussion**

### 335 *5.1 Mélange evolution and deformation mechanisms*

336 Since late Messinian times, the Mt. Massico tectonic mélange developed by out-of sequence  
337 thrusting of multiple thrust sheets above the clastic deposits and by localization of deformation at

338 the base of clastic deposits (Fig. 9a-c; Smeraglia et al., 2019). Therefore, when out-of sequence  
339 deformation initiated, WSW-ENE shortening affected W-SW-dipping (30°-55°) Meso-Cenozoic  
340 carbonates and middle-upper Miocene clastic deposits, tilted by previous thrust-related folding (Fig.  
341 2a,b and 9b; Smeraglia et al., 2019). In this context, both layer-perpendicular/oblique shortening  
342 and layer-parallel extension occurred in the early phases of deformation (Fig. 10a,b). Layer-  
343 perpendicular/oblique shortening was driven by sub-horizontal tectonic compression and produced  
344 bedding-parallel foliation by pressure-solution and stylolites generation in the marly and shaly  
345 interbeds (Figs. 3a,b). Layer-parallel extension produced dismembering, boudinage, and fracturing  
346 of competent bedding (i.e. sandstones and calcarenites interbeds; Fig. 3c).

347 With increasing deformation, the hemipelagic marls between the clastic deposits and  
348 bryozoan-rich limestones were scraped off and mixed within the base of clastic deposits, the  
349 competent beds were almost completely dismembered, although some relicts of bedding were  
350 scattered within the shaly/marly matrix (Figs. 3d, 4e-g, and 10c,d). In this framework, S-C  
351 tectonites and block-in-matrix fabric developed within the strongly deformed parts of the tectonic  
352 mélange by brittle-ductile processes such as pressure-solution, fracturing/veining, and frictional  
353 sliding, with absence of evident cataclasis of the host rock (Fig. 10c,d). The absence of cataclasis is  
354 related to the occurrence of widespread pressure solution processes, triggered and enhanced by  
355 clay-rich host rocks (marls and shales; Renard et al., 1997), which promoted the dissipation of  
356 tectonic stress through host rock dissolution, at slow strain rates rather, than frictional processes  
357 (i.e. fracturing, grain rotation, abrasion) commonly occurring during cataclasis in competent rocks,  
358 such as pure carbonates (e.g. Billi, 2010). In particular, pressure-solution was more pervasive in  
359 weak marly and shaly interbeds than in calcarenite interbeds, producing a network of stylolites  
360 aligned along S, C, and C' planes. Stylolites developed through host rock dissolution and insoluble  
361 materials (i.e. mainly phyllosilicates) concentrated within dissolution seams (Figs. 3f-h and 4a-c)  
362 (e.g. Tesi et al., 2013). Fracturing/veining processes, coupled with pressure-solution, affected the



363 relicts of competent rocks (Figs. 3f-h, 4a-d, and 10c,d). These types of deformation mechanisms  
364 commonly occur during tectonic *mélange* generation (e.g., Festa et al., 2012 for review).

365

## 366 5.2 *Vein development within the mélange*

367 The occurrence of veins perpendicular to stylolites suggests that both structures formed under  
368 the same stress regime, characterized by compression sub-perpendicular to the stylolites, thus  
369 generating mode I vein opening perpendicular to stylolites to regulate their evolution through time  
370 (Figs. 5a-c, 6d, 7c-f, and 11; e.g., Gratier et al., 2013). Veins parallel to stylolites (Figs. 6f and 7a,b)  
371 indicate opening direction parallel to the maximum compression direction and suggests vein  
372 opening under an unfavorable stress regime (i.e. opening direction should be perpendicular with  
373 respect to the maximum principal stress). In particular, development of fibrous veins (shear  
374 veins/slickenfibers) characterized by fibrous crystals perpendicular to the maximum principal stress  
375 have been observed in tectonic *mélange* and have been related to shear along pre-existing weak  
376 planes such as clay-rich stylolites, assisted by fluid overpressure (Fagereng et al., 2010).  
377 Alternatively, the unfavorable orientations between veins and tectonic stresses can be explained by  
378 episodic stress rotation within the *mélange*, vein reworking/rotation during deformation, and/or  
379 overpressured fluids that may have opened pre-existing discontinuities, such as stylolites. Although  
380 stylolites are commonly considered efficient barriers to fluid flow (Toussaint et al., 2018 for  
381 review), veins developed along stylolites (Fig. 7a,b) suggest that they can be preferential pathways  
382 for fluid redistribution, consistently with recent experimental and field evidence (e.g., Heap et al.,  
383 2014; Bruna et al., 2019). In particular, the low-permeability network generated by stylolites can  
384 favor fluid overpressure rise.

385 Stylolite steps filled by calcite crystals (Fig. 6f) suggest opening of voids (i.e. extensional  
386 pull-apart) due to slip along undulated stylolites, which promoted calcite precipitation into newly  
387 created space, a mechanism commonly occurring during slickenfiber generation (e.g. Fagereng and  
388 Byrnes, 2015). This mechanism indicates that frictional sliding occurred along S-, C-, and C'-planes

389 by smoothing the tooth-shaped margins of stylolites and slip along thick clay-rich dissolution seams  
390 (Fig. 10d; Tesei et al., 2013).

391       Fibrous crystals (Figs. 6d-f and 7a,b) generated through multiple and micrometer-thick  
392 opening increments (e.g., Bons et al., 2012), is incompatible with coeval growth of blocky and/or  
393 elongated-blocky crystals that typically develop in fluid-filled spaces generated by a single opening  
394 increment larger than that of fibrous veins (e.g. Bons et al., 2012). These different deformation  
395 mechanisms suggest various slip rates and deformation behaviors within the *mélange*. Continuous  
396 deformation may have occurred within the ductile clay-rich matrix, while discontinuous slip may  
397 have occurred during fibrous and blocky vein generation in more competent carbonate-rich blocks  
398 (e.g. Fagereng, 2011). In particular, fibrous veins suggest discontinuous creep at very slow slip  
399 rates. On the contrary, impulsive deformation at high and fast slip rates may have occurred during  
400 blocky vein generation generated by impulsive crackle-like brecciation (e.g. Woodcock et al., 2014;  
401 Fagereng and Byrnes, 2015). In both cases, fracturing/veining were probably assisted by fluid  
402 overpressure, consistently with crackle-like brecciation (Fig. 5) and the dense network of clay-rich  
403 stylolites, which may have created impermeable barriers and fluid pressure rises over time (Moore  
404 and Vrolijk, 1992).

405       Crosscutting relationships between structures show recurrent cycles of mutually overprinting  
406 brittle (fracturing/veining and frictional sliding) and ductile (pressure-solution) processes indicate a  
407 multiphase deformation history (Figs. 5, 6, 7, and 11). Stylolite formation through fibrous veins  
408 (Fig. 6d,e) indicate the interruption of the fracturing event and the onset of a new pressure-solution  
409 phase, indicating alternating phases of frictional sliding and dissolution processes (Fig. 11; e.g.,  
410 Tesei et al., 2013; Giorgetti et al., 2016). Reworking of inherited veins also occurred (Figs. 10b and  
411 11). This inference is consistent with previous U/Pb dating on three calcite-filled veins within the  
412 tectonic *mélange* showing ages of  $10.5 \pm 2.5$  My,  $7.0 \pm 1.6$  My, and  $5.1 \pm 3.7$  My, respectively  
413 indicating multiple events of calcite precipitation during deformation (Smeraglia et al., 2019).

414

### 415 5.3 Fluid source and syn-tectonic fluid circulation

416 Geochemical data indicate calcite precipitation at temperatures between ~100 and ~150 °C  
417 from retained pore water, such as marine water retained in the clastic sediments during diagenesis,  
418 modified or completely buffered by isotope exchange with the host rock. We base this interpretation  
419 on the following evidence:

420 (1) The calculated  $\delta^{18}\text{O}$  paleofluid composition, which was in equilibrium with the calcite at  
421 the time of mineral growth, ranges between +9.1‰ and +13.7‰ (Fig. 8b). These values indicate  
422  $^{18}\text{O}$  enrichment suggesting extensive oxygen exchange between the fluids and the limestone  
423 interbeds of clastic deposits. In particular, most of the calculated paleofluid compositions  
424 ranging between +9‰ and +11‰ (Fig. 8b), indicate high water/rock ratios and paleofluids with  
425 nearly constant  $\delta^{18}\text{O}$  composition, which were responsible for calcite precipitation at progressive  
426 increasing temperatures from 108 to 146 °C (Fig. 8b).

427 (2) Data from fluid inclusions in veins suggest an excess of radiogenic He and Ar in fluids  
428 circulating during the precipitation of calcite, indicating a source of both He and Ar other than the  
429 atmosphere and the mantle. In particular, the  $^3\text{He}/^4\text{He}$  ratios are lower than 0.1 R/Ra (Fig. 8d and  
430 Table S3) indicating a crustal fluid. In addition, these values are similar to those of crustal-derived  
431 fluids (with limited or negligible mantle contribution) enriched in  $^4\text{He}$  recorded in natural gaseous  
432 emissions of the central-northern Apennines (e.g., Buttitta et al., 2020).

433 (3) The R/Ra ratios of calcite veins are lower than those calculated from actual springs along  
434 the Mt. Massico ridge and related to the Roccamonfina volcano (0.39 Ra to 1.99 Ra, typical of  
435 mantle-derived fluids; Cuoco et al., 2017), located ~20 towards the NE respect to the study area  
436 (Fig. 1), thus excluding the contribution of mantle-derived fluids circulating within the tectonic  
437 mélange. In addition, the volcanic activity at Roccamonfina occurred between ~0.6 and ~0.1 My,  
438 ~5 My after the latest tectonic activity documented at Mt. Massico (U-Pb vein dated at  $5.1 \pm 3.7$   
439 My, Smeraglia et al., 2019), further excluding the mixing of mantle-derived fluids from  
440 Roccamonfina with crustal fluids circulated within the tectonic mélange.

441        However, we cannot completely exclude that also meteoric water partly infiltrated within the  
442 tectonic *mélange* during deformation and/or exhumation, and was modified by  $^{18}\text{O}$  isotope  
443 exchange with the host rock, acquiring the calculated  $\delta^{18}\text{O}$  paleofluid composition.

444        Based on geochemical and geological data, we suggest that syn-tectonic fluid circulation  
445 within the Mt. Massico *mélange* occurred in a closed system, without a strong connection with  
446 external reservoirs (i.e. meteoric or mantle-derived fluids). We therefore propose that during  
447 sedimentary and tectonic burial, marine-derived fluids trapped within sandstones and shale  
448 interlayers were progressively heated up to 147 °C. During deformation, regional tectonic  
449 shortening caused sandstones and shale compaction, porosity reduction, and, eventually, expulsion  
450 of previously stored fluids and calcite precipitation into newly-created fractures. In addition, the  
451 progressive smectite to illite conversion through mixed layers illite-smectite occurring from  
452 temperatures of 60-70 °C to 210 °C (Aldega et al., 2017), may have triggered additional source for  
453 local fluids due to water expulsion during clay dehydration (e.g. Moore and Vrolijk, 1992).

454        Syn-tectonic fluid circulation in closed systems has been already observed in tectonic  
455 *mélange* exposed in various fold-and-thrust belts (i.e. Apennines, Pyrenees) developed within  
456 sedimentary succession with alternating of sandstones, marls, and shale (e.g., Vannucchi et al,  
457 2010; Gabellone et al., 2013; Lacroix et al., 2014). The Mt. Massico *mélange* did not acted as a  
458 conduit for external fluids as observed within intra-wedge tectonic *mélange* in the Apennines  
459 (Meneghini et al., 2012), Sicilian (Dewever et al., 2013), Thailand (Hansberry et al., 2015), and  
460 Japan (Raimbourg et al., 2015) fold-and-thrust belts. We explain this difference suggesting that  
461 meso- and microstructures of the Mt. Massico *mélange*, such as clay-rich stylolites and marls-shale  
462 interlayers (Figs. 3, 4, 6, and 7), created efficient low-permeability barriers, which prevented the  
463 ingress of fluids from external reservoirs. Otherwise, the occurrence of regional thrusts, both below  
464 and above the Mt. Massico tectonic *mélange*, may have acted as regional conduits for the drainage  
465 of external fluids within the accretionary wedge and away from the tectonic *mélange*.

466 We observe an inverse correlation between fluid temperature and ages of calcite veins,  
467 showing an increase of calcite precipitation temperature with decreasing ages (Fig. 8c; U-Pb data  
468 from Smeraglia et al., 2019). The vein formed at  $10.5 \pm 2.5$  My at temperature of 108 °C suggests  
469 an early phase of deformation during wedge accretion (e.g. Tavani et al., 2015). This is not  
470 consistent with the burial history proposed by Smeraglia et al. (2019), which shows much lower  
471 temperature for the base of the clastic deposits than that recorded by clumped isotopes before the  
472 onset of thrusting at  $10.5 \pm 2.5$  My (i.e. Tortonian time; see Fig. 13a in Smeraglia et al., 2019). This  
473 can be explained by the lateral and upward migration of deep-seated warm fluids, previously stored  
474 in areas already affected by tectonic burial (e.g., Minshull et al., 1989), which circulated within the  
475 clastic deposits at shallow depths during the Tortonian. The occurrence pre-Tortonian tectonic  
476 burial is highlighted by the borehole stratigraphy of Mara 01 well, located towards the SW respect  
477 the Mt. Massico, showing the thrusting of Triassic deposits above Paleocene-Eocene deposits (See  
478 Fig. 2 in Smeraglia et al., 2019)

479 Veins formed at  $7.0 \pm 1.6$  My and  $5.1 \pm 3.7$  My at temperatures of 121 and 147 °C,  
480 respectively, are consistent with the progressive burial due to thrust sheet emplacement above the  
481 *mélange* (Smeraglia et al., 2019). However, we point out that most of precipitation temperatures are  
482 fully consistent with the maximum burial temperature of 140 °C at depths of ~4 km experienced by  
483 the *mélange*, calculated by 1D thermal modelling constrained by mixed layers illite-smectite  
484 (Smeraglia et al., 2019). This indicates that fluid expulsion occurred under maximum burial  
485 condition, suggesting that tectonic overburden promoted and/or triggered fluid overpressure and  
486 hydrofracturing.

487

## 488 **Conclusions**

489 Structural and microstructural observations combined with geochemical data (stable and  
490 clumped isotopes and isotope composition of noble gases in fluid inclusions of calcite veins) along

491 the carbonate/shale-bearing tectonic mélange within the central Apennines accretionary wedge (Mt.  
492 Massico mélange) show that:

493 (1) Intra-wedge tectonic mélange generates along pre-existent intra- and interformational  
494 rheological contrast occurring along carbonate/shale sedimentary successions. In particular,  
495 deformation is localized at the boundary between weak (Tortonian clastic deposits and hemipelagic  
496 marls) and competent (Meso-Cenozoic limestones) rocks. The development of tectonic mélange  
497 occurred by disruption of the primary bedding, mixing, and deformation of relicts of competent  
498 blocks (i.e., olistoliths and relicts of competent strata) within a weak matrix (i.e., deformed shaly  
499 and marly interbeds), through recurrent cycles of mutually overprinting brittle (fracturing/veining  
500 and frictional sliding) and ductile (pressure-solution) processes, indicating a polyphase deformation  
501 history characterized by fast to slow strain rates.

502 (2) The geochemical signatures of syn-tectonic calcite veins indicate calcite precipitation  
503 from warm (108-147 °C) and modified pore fluids, by isotope exchange with the local host rock.  
504 Fluid circulation occurred mostly in a closed system dominated by the expulsion and redistribution  
505 of pore fluids trapped during sedimentation/diagenesis and/or derived by clay dehydration processes  
506 (at  $T > 120$  °C), without the interaction of externally derived fluids (i.e. meteoric and/or mantle-  
507 derived fluids). A minor contribution from lateral-upward migration of deep-seated warm fluids,  
508 previously stored in areas affected by tectonic burial located towards the SW from the Mt. Massico,  
509 is inferred in the early phase of the deformation of tectonic mélange. Low-permeability barriers,  
510 generated by clay-rich stylolites, promoted the generation of fluid overpressure, which were mostly  
511 expelled at maximum burial conditions ( $T$  140 °C and depth of ~4 km) in the final stage of mélange  
512 deformation. Therefore, clay-rich intra-wedge tectonic mélanges, along décollement zones, may  
513 generate efficient barriers within accretionary wedges for vertical and lateral redistribution of fluids  
514 from reservoirs outside the mélange.

515

516 We highlight that the integration of geochemical (stable and clumped isotopes, analysis of  
517 gaseous species in fluid inclusions) and geochronological (U-Pb dating) methods can be a powerful  
518 approach to better constrain the burial-thermal evolution and the fluid storage capacity of fold and  
519 thrust belts and sedimentary basins, including the associated fault network.

520

## 521 **Acknowledgements**

522 This work has been funded by: Progetti di Ateneo Sapienza 2017 to E. Carminati, Progetti di  
523 Ateneo Sapienza 2016 to L. Aldega, and Progetto di Avvio alla Ricerca 2016 Sapienza to L.  
524 Smeraglia. We thank D. Mannelta and TSLab & Geoservices for thin sections, A. Conti, F. Di  
525 Fiore, and S. Fabbi constructive discussions and help during fieldwork and sampling and M. Jaggi  
526 for the isotope analyses. We are grateful to M. Tantillo for analyzing the chemistry of CO<sub>2</sub>+H<sub>2</sub>O,  
527 N<sub>2</sub>, and the isotope composition of light noble gases.

528

## 529 **References**

- 530 Aldega L., Carminati E., Scharf A., Mattern F. & Al-Wardi M. (2017). Estimating original  
531 thickness and extent of the Semail Ophiolite in the eastern Oman Mountains by paleothermal  
532 indicators. *Marine and Petroleum Geology*, 84, 18-33.
- 533 Bernasconi, S. M., Müller, I. A., Bergmann, K. D., Breitenbach, S. F., Fernandez, A., et al. (2018).  
534 Reducing uncertainties in carbonate clumped isotope analysis through consistent  
535 carbonate-based standardization. *Geochemistry, Geophysics, Geosystems*, 19(9), 2895-2914.
- 536 Billi, A. (2010). Microtectonics of low-P low-T carbonate fault rocks. *Journal of Structural*  
537 *Geology*, 32(9), 1392-1402.
- 538 Billi, A., Bosi, V., & De Meo, A. (1997). Caratterizzazione strutturale del rilievo del M. Massico  
539 nell'ambito dell'evoluzione quaternaria delle depressioni costiere dei fiumi Garigliano e  
540 Volturno (Campania settentrionale). *Il Quaternario*, 10(1), 15–26.

541 Bons, P. D., Elburg, M. A., & Gomez-Rivas, E. (2012). A review of the formation of tectonic veins  
 542 and their microstructures. *Journal of Structural Geology*, 43, 33-62.

543 Bruna, P. O., Lavenu, A. P., Matonti, C., & Bertotti, G. (2019). Are stylolites fluid-flow efficient  
 544 features?. *Journal of Structural Geology*, 125, 270-277.

545 Buttitta, D., Caracausi, A., Chiaraluce, L., Favara, R., Morticelli, M. G., & Sulli, A. (2020).  
 546 Continental degassing of helium in an active tectonic setting (northern Italy): the role of  
 547 seismicity. *Scientific Reports*, 10(1), 1-13.

548 Carminati, E., Lustrino, M., & Doglioni, C. (2012). Geodynamic evolution of the central and  
 549 western Mediterranean: Tectonics vs. igneous petrology constraints. *Tectonophysics*,  
 550 579, 173–192. <https://doi.org/10.1016/j.tecto.2012.01.026>

551 Codegone, G., Festa, A., & Dilek, Y. (2012). Formation of Taconic mélanges and broken  
 552 formations in the Hamburg Klippe, central Appalachian orogenic belt, eastern Pennsylvania.  
 553 *Tectonophysics*, 568, 215-229.

554 Cuoco, E., Minissale, A., Tamburrino, S., Iorio, M., & Tedesco, D. (2017). Fluid geochemistry of  
 555 the Mondragone hydrothermal systems (southern Italy): water and gas compositions vs.  
 556 geostructural setting. *International Journal of Earth Sciences*, 106(7), 2429-2444.

557 Dennis, K. J., Affek, H. P., Passey, B. H., Schrag, D. P., & Eiler, J. M. (2011). Defining an absolute  
 558 reference frame for ‘clumped’ isotope studies of CO<sub>2</sub>. *Geochimica et Cosmochimica Acta*,  
 559 75(22), 7117-7131.

560 Dewever, B., Swennen, R., & Breesch, L. (2013). Fluid flow compartmentalization in the Sicilian  
 561 fold and thrust belt: Implications for the regional aqueous fluid flow and oil migration history.  
 562 *Tectonophysics*, 591, 194-209.

563 Di Girolamo, P., Sgroso, I., De Gennaro, R., & Giurazzi, S. (2000). Metamorphic rocks in  
 564 Campania (southern Italy); The “Mondragone marbles”. *Bollettino della Societa Geologica*  
 565 *Italiana*, 119(3), 761–766.



566 Fagereng, Å. (2011). Fractal vein distributions within a fault-fracture mesh in an exhumed  
567 accretionary mélange, Chrystalls Beach Complex, New Zealand. *Journal of Structural*  
568 *Geology*, 33(5), 918-927.

569 Fagereng, Å., & Byrnes, G. (2015). A range of fault slip styles on progressively misoriented planes  
570 during flexural-slip folding, Cape Fold Belt, South Africa. *Journal of Structural Geology*, 70,  
571 156-169.

572 Fagereng, Å., & Cooper, A. F. (2010). The metamorphic history of rocks buried, accreted and  
573 exhumed in an accretionary prism: An example from the Otago Schist, New Zealand. *Journal*  
574 *of Metamorphic Geology*, 28(9), 935–954. <https://doi.org/10.1111/j.1525-1314.2010.00900.x>

575 Fagereng, Å., Remitti, F., & Sibson, R. H. (2010). Shear veins observed within anisotropic fabric at  
576 high angles to the maximum compressive stress. *Nature Geoscience*, 3(7), 482.

577 Festa, A., Dilek, Y., Pini, G. A., Codegone, G., & Ogata, K. (2012). Mechanisms and processes of  
578 stratal disruption and mixing in the development of mélanges and broken formations:  
579 Redefining and classifying mélanges. *Tectonophysics*, 568, 7-24.

580 Gabellone, T., Gasparri, M., Iannace, A., Invernizzi, C., Mazzoli, S., & D'antonio, M. (2013).  
581 Fluid channeling along thrust zones: the Lagonegro case history, southern Apennines, Italy.  
582 *Geofluids*, 13(2), 140-158.

583 Giorgetti, C., Collettini, C., Scuderi, M. M., Barchi, M. R., & Tesei, T. (2016). Fault geometry and  
584 mechanics of marly carbonate multilayers: An integrated field and laboratory study from the  
585 Northern Apennines, Italy. *Journal of Structural Geology*, 93, 1-16.

586 Gratier, J. P., Thouvenot, F., Jenatton, L., Tourette, A., Doan, M. L., & Renard, F. (2013).  
587 Geological control of the partitioning between seismic and aseismic sliding behaviours in  
588 active faults: Evidence from the Western Alps, France. *Tectonophysics*, 600, 226-242.

589 Hansberry, R. L., Collins, A. S., King, R. C., Morley, C. K., Gize, A. P., Warren, J., ... & Hall, P. A.  
590 (2015). Syn-deformation temperature and fossil fluid pathways along an exhumed detachment  
591 zone, khao khwang fold-thrust belt, Thailand. *Tectonophysics*, 655, 73-87.

592 Heap, M. J., Baud, P., Reuschlé, T., & Meredith, P. G. (2014). Stylolites in limestones: Barriers to  
 593 fluid flow?. *Geology*, 42(1), 51-54.

594 Hilgen, F., Aziz, H. A., Bice, D., Iaccarino, S., Krijgsman, W., Kuiper, K., ... & Zachariasse, W. J.  
 595 (2005). The global boundary stratotype section and point (GSSP) of the Tortonian stage  
 596 (Upper Miocene) at Monte Dei Corvi. *Episodes-Newsmagazine of the International Union of*  
 597 *Geological Sciences*, 28(1), 6-17.

598 Lacroix, B., Travé, A., Buatier, M., Labaume, P., Vennemann, T., & Dubois, M. (2014).  
 599 Syntectonic fluid-flow along thrust faults: Example of the South-Pyrenean fold-and-thrust  
 600 belt. *Marine and Petroleum Geology*, 49, 84-98.

601 Luiso, P., Paoletti, V., Nappi, R., La Manna, M., Cella, F., Gaudiosi, G., & Iorio, M. F. M. (2018).  
 602 A multidisciplinary approach to characterize the geometry of active faults: The example  
 603 of Mt. Massico, Southern Italy. *Geophysical Journal International*, 213(3), 1673–  
 604 1681. <https://doi.org/10.1093/gji/ggy080>

605 Malinverno, A., & Ryan, W. B. (1986). Extension in the Tyrrhenian Sea and shortening in the  
 606 Apennines as result of arc migration driven by sinking of the lithosphere. *Tectonics*,  
 607 5(2), 227–245. <https://doi.org/10.1029/TC005i002p00227>

608 Meneghini, F., Marroni, M., Moore, J. C., Pandolfi, L., & Rowe, C. D. (2009). The processes of  
 609 underthrusting and underplating in the geologic record: Structural diversity between  
 610 the Franciscan Complex (California), the Kodiak Complex (Alaska) and the Internal  
 611 Ligurian Units (Italy). *Geological Journal*, 44(2), 126–152. <https://doi.org/10.1002/gj.1144>

612 Meneghini, F., Botti, F., Aldega, L., Boschi, C., Corrado, S., Marroni, M., & Pandolfi, L. (2012).  
 613 Hot fluid pumping along shallow-level collisional thrusts: the Monte Rentella Shear Zone,  
 614 Umbria Apennine, Italy. *Journal of Structural Geology*, 37, 36-52.

615 Minshull, T., & White, R. (1989). Sediment compaction and fluid migration in the Makran  
 616 accretionary prism. *Journal of Geophysical Research: Solid Earth*, 94(B6), 7387-7402.

617 Moore, J. C., & Vrolijk, P. (1992). Fluids in accretionary prisms. *Reviews of Geophysics*, 30(2),  
618 113-135.

619 Morley, C. K., von Hagke, C., Hansberry, R. L., Collins, A. S., Kanitpanyacharoen, W., & King, R.  
620 (2017). Review of major shale-dominated detachment and thrust characteristics in the  
621 diagenetic zone: Part I, meso-and macro-scopic scale. *Earth-Science Reviews*, 173, 168–228.  
622 <https://doi.org/10.1016/j.earscirev.2017.07.019>

623 Mostardini, F., & Merlini, S. (1986). Appennino centroemeridionale. Sezioni geologiche e proposta  
624 di modello strutturale. *Memorie della Societa Geologica Italiana*, 35, 177–202.

625 O'Neil, J. R., Clayton, R. N., & Mayeda, T. K. (1969). Oxygen isotope fractionation in divalent  
626 metal carbonates. *The Journal of Chemical Physics*, 51(12), 5547-5558.

627 Ogata, K., Pini, G. A., Carè, D., Zélic, M., & Dellisanti, F. (2012). Progressive development of  
628 block-in-matrix fabric in a shale-dominated shear zone: Insights from the Bobbio  
629 Tectonic Window (Northern Apennines, Italy). *Tectonics*, 31, TC1003. [https://](https://doi.org/10.1029/2011TC002924)  
630 [doi.org/10.1029/2011TC002924](https://doi.org/10.1029/2011TC002924)

631 Raimbourg, H., Augier, R., Famin, V., Gadenne, L., Palazzin, G., Yamaguchi, A., & Kimura, G.  
632 (2014). Long-term evolution of an accretionary prism: The case study of the Shimanto Belt,  
633 Kyushu, Japan. *Tectonics*, 33(6), 936-959.

634 Renard, F., Ortoleva, P., & Gratier, J. P. (1997). Pressure solution in sandstones: influence of clays  
635 and dependence on temperature and stress. *Tectonophysics*, 280(3-4), 257-266.

636 Sgroso, I. (1974). I rapporti tra la piattaforma carbonatica Campano-Lucana e la piattaforma  
637 Abruzzese-Campana al Monte Massico (Caserta). *Bollettino della Societa Geologica Italiana*,  
638 93(4), 1197–1209.

639 Smeraglia, L., Aldega, L., Billi, A., Carminati, E., Di Fiore, F., Gerdes, A., ... & Vignaroli, G.  
640 (2019). Development of an Intrawedge Tectonic Mélange by Out-of-Sequence Thrusting,  
641 Buttressing, and Intraformational Rheological Contrast, Mt. Massico Ridge, Apennines, Italy.  
642 *Tectonics*, 38(4), 1223-1249.

643 Tavani, S., Storti, F., Lacombe, O., Corradetti, A., Muñoz, J. A., & Mazzoli, S. (2015). A review of  
644 deformation pattern templates in foreland basin systems and fold-and-thrust belts:  
645 Implications for the state of stress in the frontal regions of thrust wedges. *Earth-Science*  
646 *Reviews*, 141, 82-104.

647 Tesei, T., Collettini, C., Viti, C., & Barchi, M. R. (2013). Fault architecture and deformation  
648 mechanisms in exhumed analogues of seismogenic carbonate-bearing thrusts. *Journal of*  
649 *Structural Geology*, 55, 167-181.

650 Toussaint, R., Aharonov, E., Koehn, D., Gratier, J. P., Ebner, M., et al. (2018). Stylolites: A review.  
651 *Journal of Structural Geology* 114, 163-195.

652 Vannucchi, P., & Bettelli, G. (2002). Mechanism of subduction accretion as implied from the  
653 broken formations in the Apennines, Italy. *Geology*, 30(9), 835–  
654 838. [https://doi.org/10.1130/0091-7613\(2002\)030<0835:MOSAAI>2.0.CO;2](https://doi.org/10.1130/0091-7613(2002)030<0835:MOSAAI>2.0.CO;2)

655 Vannucchi, P., Remitti, F., & Bettelli, G. (2008). Geological record of fluid flow and seismogenesis  
656 along an erosive subducting plate boundary. *Nature*, 451(7179), 699–  
657 703. <https://doi.org/10.1038/nature06486>

658 Vannucchi, P., Remitti, F., Bettelli, G., Boschi, C., & Dallai, L. (2010). Fluid history related to the  
659 early Eocene-middle Miocene convergent system of the Northern Apennines  
660 (Italy): Constraints from structural and isotopic studies. *Journal of Geophysical*  
661 *Research*, 115, B05405. <https://doi.org/10.1029/2009JB006590>

662 Vezzani, L., Festa, A., & Ghisetti, F. C. (2010). Geology and tectonic evolution of the  
663 Central-Southern Apennines, Italy, Special Paper (Vol. 469, pp. 1–58). America: Geological  
664 Society. <https://doi.org/10.1130/2010.2469>

665 Vitale, S., & Ciarcia, S. (2018). Tectono-stratigraphic setting of the Campania region (southern  
666 Italy). *Journal of Maps*, 14(2), 9–21. <https://doi.org/10.1080/17445647.2018.1424655>

667 Vitale, S., Prinzi, E. D., Ciarcia, S., Sabbatino, M., Tramparulo, F. D. A., & Verrazzo, G. (2018).  
668 Polyphase out-of-sequence thrusting and occurrence of marble detritus within the wedge-top

669 basin deposits in the Mt. Massico (southern Apennines): Insights into the late  
670 Miocene tectonic evolution of the central Mediterranean. *International Journal of Earth*  
671 *Sciences*. <https://doi.org/10.1007/s00531-018-1664-0>

672 Vrolijk, P., Myers, G., & Moore, J. C. (1988). Warm fluid migration along tectonic melanges in the  
673 Kodiak accretionary complex, Alaska. *Journal of Geophysical Research: Solid Earth*,  
674 93(B9), 10313-10324.

675 Woodcock, N. H., Miller, A. V. M., & Woodhouse, C. D. (2014). Chaotic breccia zones on the  
676 Pembroke Peninsula, south Wales: Evidence for collapse into voids along dilational faults.  
677 *Journal of Structural Geology*, 69, 91-107.

678

## 679 **Figure Captions**

680 **Figure 1. (a)** Simplified geological map of the central-southern Apennines (Italy) showing main  
681 thrusts and location of the study area. **(b)** Schematic geological cross-section through  
682 the central-southern Apennines (modified after Mostardini and Merlini, 1986). **(c)**  
683 Geological cross-section through the Mt. Massico ridge (i.e., the study area).

684

685 **Figure 2. (a)** Detailed geological map of the southwestern part of the Mt. Massico ridge with  
686 location of key outcrops where the tectonic mélange is exposed. Schmidt nets  
687 (lower hemisphere) showing the attitude of S-C planes with related slip vectors within the  
688 tectonic mélange. Modified after Smeraglia et al. (2019) **(b)** Geological cross-sections  
689 across the Mt. Massico ridge.

690

691 **Figure 3.** Outcrop-scale structural features of the Mt. Massico tectonic mélange. **(a,b)** The poorly  
692 deformed clastic deposits showing bedding and incipient foliation. Note folded strata and  
693 low-displacement faults showing ramp and flat geometry. **(c)** The moderately deformed zone  
694 showing competent strata (i.e. sandstones and calcarenites interbeds) characterized by pinch-

and-swell and boudine-like geometries. **(d)** Relict of competent strata. **(d)** Detail of competent strata (Fig. 3c) showing veins perpendicular to bedding and S-C foliation. **(f,g)** The strongly deformed part of the tectonic *mélange* showing S-C foliation within marls and shale and relict of competent strata (limestones and sandstones) showing sigmoidal shapes. **(h)** Relict of competent limestones showing stylolites along S- and C-planes. Inset shows the Schmidt nets (lower hemisphere) showing the attitude of S-C planes with related slip vectors.

**Figure 4.** Outcrop-scale structural features of the Mt. Massico tectonic *mélange*. **(a-c)** The strongly deformed part of the tectonic *mélange* characterized by S-C and S-CC' tectonites within marls and shale and relict of competent strata (limestones and sandstones) showing sigmoidal shapes. **(d)** Relict of competent limestones showing a pervasive network of calcite veins. **(e-h)** Inherited competent (limestones) olistoliths scattered within the weak (marls and shale) scaly foliation, generating the block-in-matrix fabric typical of tectonic *mélange*. **(h)** Contorted and convoluted foliation within the S-C tectonite.

**Figure 5.** High-resolution hand sample scan of relicts of competent limestones showing sigmoidal shapes. Stylolites are aligned along S-, C- and C'-planes. Calcite veins are oriented parallel, perpendicular, and/or oblique with respect to stylolites. No stylolites affecting calcite veins and calcite veins cutting through stylolites occur.

**Figure 6.** Microstructures from the tectonic *mélange*. **(a-c)** Stylolites affecting host rock relicts and calcite veins. Note the insoluble materials (clays and oxides) filling up to 1-mm thick dissolution seams. **(d,e)** Fibrous veins characterized by fibrous calcite crystals with long axis oriented roughly parallel to stylolites. Note stylolites affecting fibrous veins. **(f)** Fibrous crystals developed along stylolites jogs along C-plane. Fibrous crystals with long axis oriented roughly parallel to stylolites.

721

722 **Figure 7.** Microstructures from the tectonic mélange. **(a,b)** Fibrous veins characterized by fibrous  
723 calcite crystals with long axis oriented perpendicular to stylolites. Note that this type of  
724 fibrous veins develop within stylolites. **(c,d,e,f)** Blocky veins characterized by blocky calcite  
725 crystals. Blocky veins are oriented parallel, perpendicular, and/or oblique respect to stylolites.  
726 Note stylolites affecting blocky veins and mutual crosscutting relationships between blocky  
727 veins.

728

729 **Figure 8.** **(a)**  $\delta^{13}\text{C}$  (‰ V-PDB) versus  $\delta^{18}\text{O}$  (‰ V-SMOW) diagram from blocky and fibrous veins  
730 and host rocks in the Mt. Massico tectonic mélange. Notice the average  $\delta^{18}\text{O}$  depletion of  
731  $\sim 4\text{‰}$  between mélange-related mineralizations and host rock. **(b)** Oxygen isotope  
732 fractionation during equilibrium precipitation:  $\delta^{18}\text{O}$  of fault-related mineralizations and  
733 paleofluid compositions (curves) as a function of temperature. The  $\delta^{18}\text{O}$  calculated paleofluid  
734 compositions (between 9‰ and 14‰) indicate strong  $^{18}\text{O}$  exchange with the local limestone  
735 host rock. Notice that warmer fluids have similar  $\delta^{18}\text{O}$  paleofluid composition suggesting that  
736 the same paleofluid was the source for calcite precipitation at increasing temperatures and  
737 depths. **(c)** Temperature ( $^{\circ}\text{C}$ , clumped isotopes) versus age (My, U-Pb dating, data  
738 from Smeraglia et al., 2019) diagram for three dated veins. Notice the increase in  
739 paleofluid temperature with decreasing ages, which indicates progressive tectonic  
740 burial during discontinuous thrust sheet emplacement through time. **(d)**  $^4\text{He}/^{20}\text{Ne}$  ratio  
741 versus  $^3\text{He}/^4\text{He}$  (R/Ra) ratio diagram. Note that the calcite veins are in the range of R/Ra  
742 values typical of crustal fluids of the central Apennines.

743

744 **Figure 9.** **(a)** Large-scale tectonic setting of the Apennine subduction (modified after Scrocca et al.,  
745 2005) and location of the Mt. Massico structure within the accretionary prism. **(b-c)**  
746 Simplified sketch showing the main sedimentary and tectonic events in the Mt. Massico area

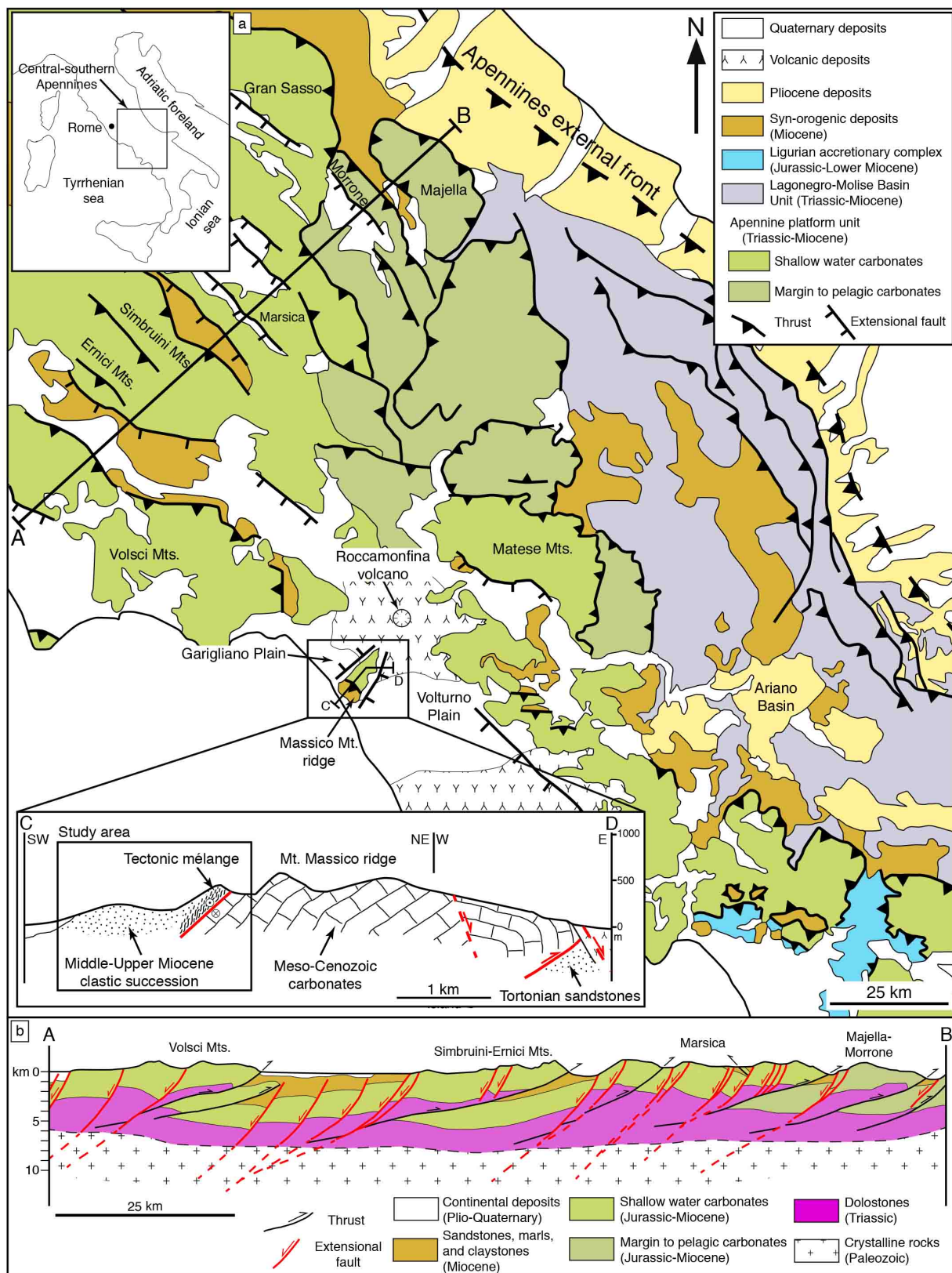
(Modified after Smeraglia et al., 2019): **(b)** During late Tortonian-early Messinian times, orogenic compression generated a fault propagation anticline located in the northeastern part of the Mt. Massico ridge, juxtaposing pre-orogenic limestones in the hangingwall with syn-orogenic Tortonian sandstones in the footwall. **(c)** During late Messinian-early Pliocene times, out-of-sequence thrusting occurred and a ~3,300 m-thick stack of imbricate thrust sheets thrust onto the Tortonian-lower Messinian clastic deposits and calcarenites. At this stage the tectonic *mélange* develop at the base of the clastic deposits. Notice that remnants of such thrust sheets are located in the Mt. Petrino area (Fig. 2).

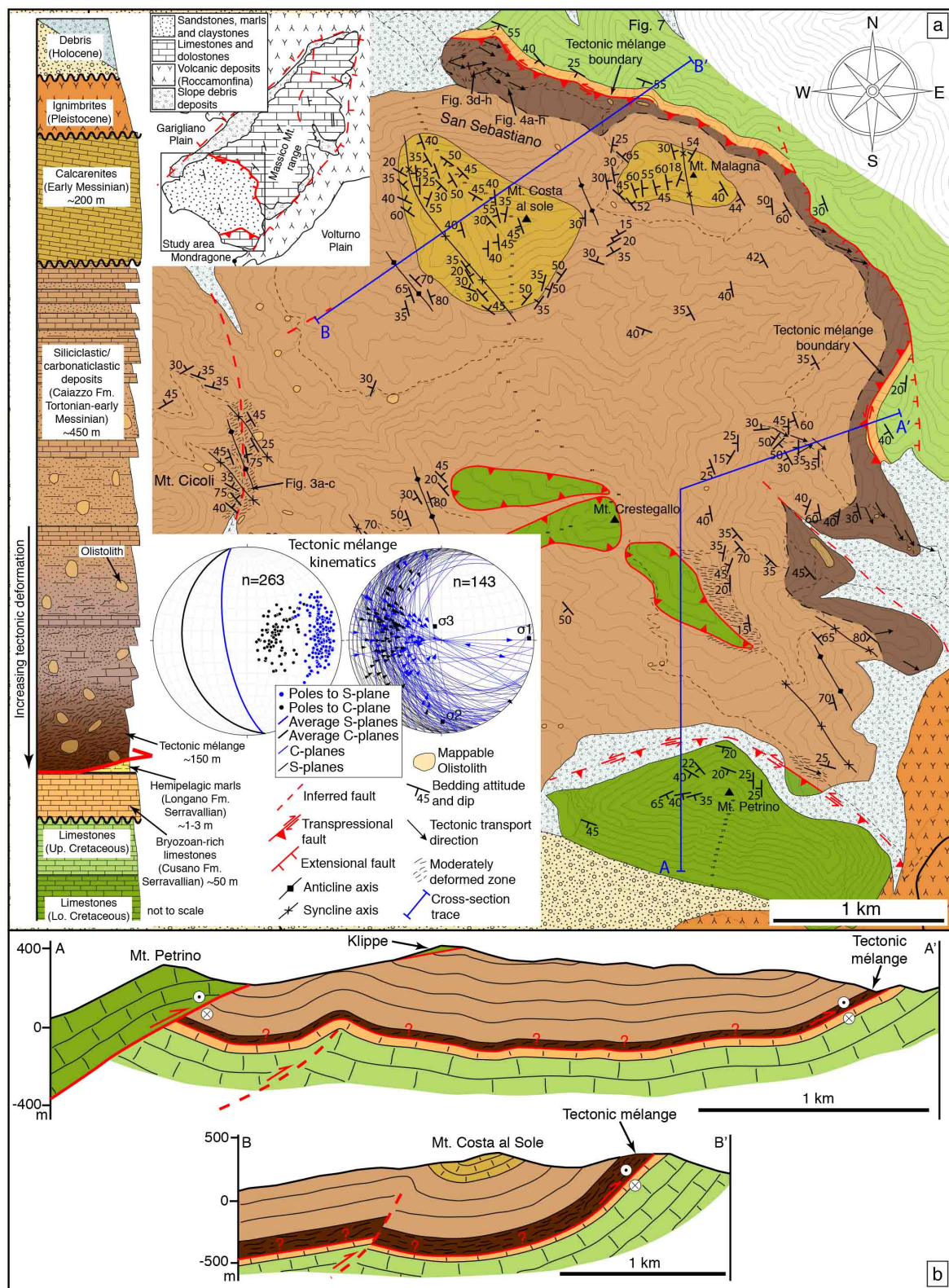
**Figure 10.** Simplified evolution of the Mt. Massico tectonic *mélange* (See Fig. 10b,c for the structural location of the evolution scheme). **(a)** During the early deformation stage, veins perpendicular to bedding develop within the clastic deposits in response to far field tectonic stress. **(b)** Initial shortening affect the clastic deposits generating a weak scaly foliation parallel respect to bedding (see Fig. 3a,b). **(c)** Progressive shortening generated S-C fabric and boudinage of competent bedding (limestones and sandstones). **(d)** During the late stage of deformation, the strongly deformed tectonic *mélange* develop. In particular, pervasive S-C tectonites develop within the weak (marls and shale) matrix and relicts of competent strata are deformed generating scattered clasts with sigmoidal shape. Notice that hemipelagic marls are scraped off and mixed within the tectonic *mélange*, while the underlying Meso-Cenozoic limestones are not deformed. The inset shows the different type of veins within the *mélange* (blocky and fibrous) and their structural position respect to stylolites.

**Figure 11.** Schematic evolutionary model for *mélange*-related veins evolution through time. Notice alternate cycles of mutually overprinting brittle (fracturing/veining) and ductile (pressure-solution and stylolites generation) processes.

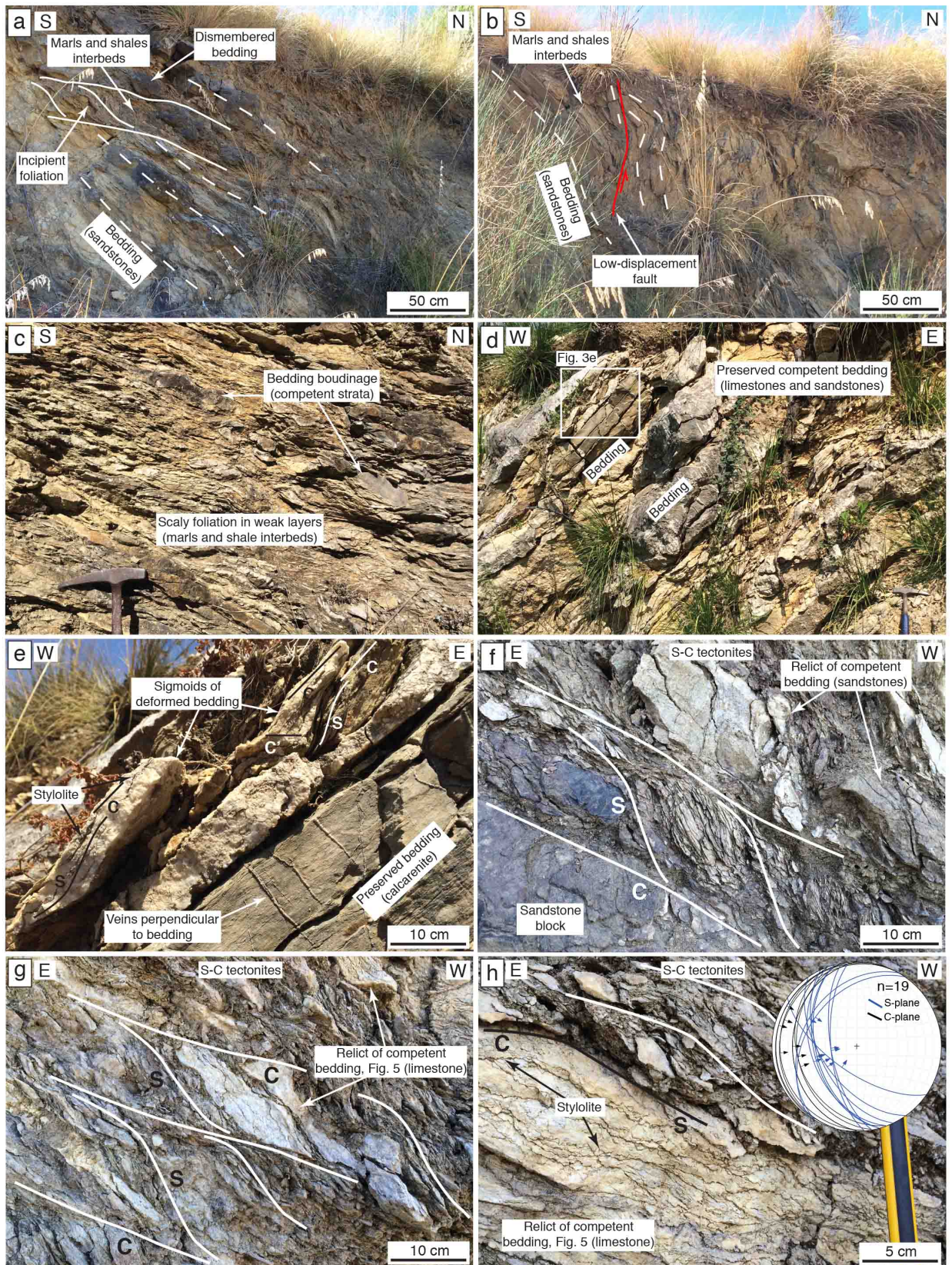


773 **Figure S1. (a)**  $^{40}\text{Ar}$  concentration versus age diagram. Notice that there is no correlation between  
774  $^{40}\text{Ar}$  concentration and ages of dated veins. **(b)**  $^4\text{He}$  concentration versus age diagram. Notice  
775 that there is no correlation between  $^4\text{He}$  concentration and ages of dated veins. **(c)**  $^3\text{He}$   
776 concentration versus age diagram. Notice that there is no correlation between  $^3\text{He}$   
777 concentration and ages of dated veins. **(d)**  $^3\text{He}/^4\text{He}$  ratio (R/Ra) versus age diagram. Notice  
778 that there is no correlation between  $^3\text{He}/^4\text{He}$  ratio (R/Ra) and ages of dated veins.

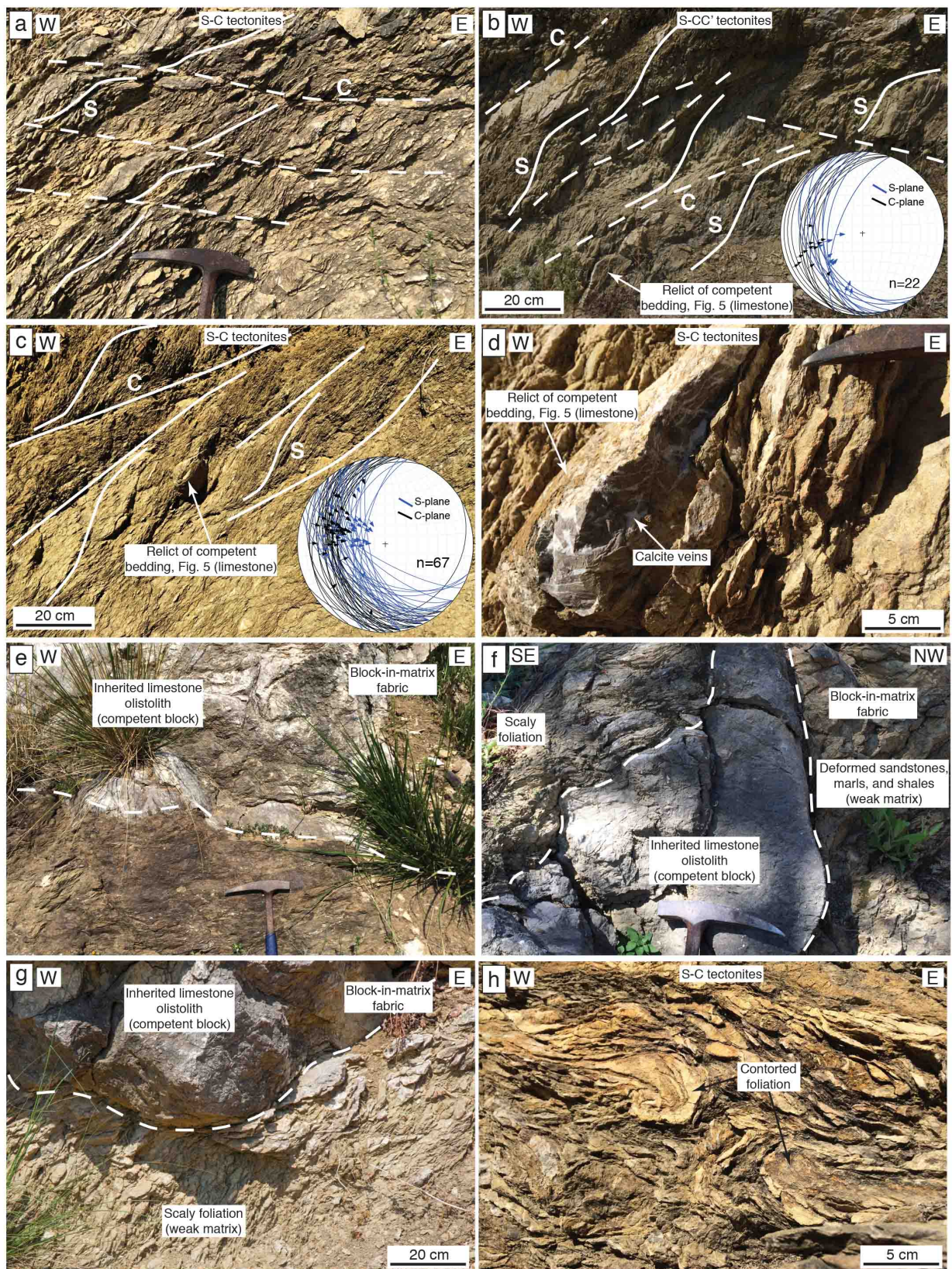






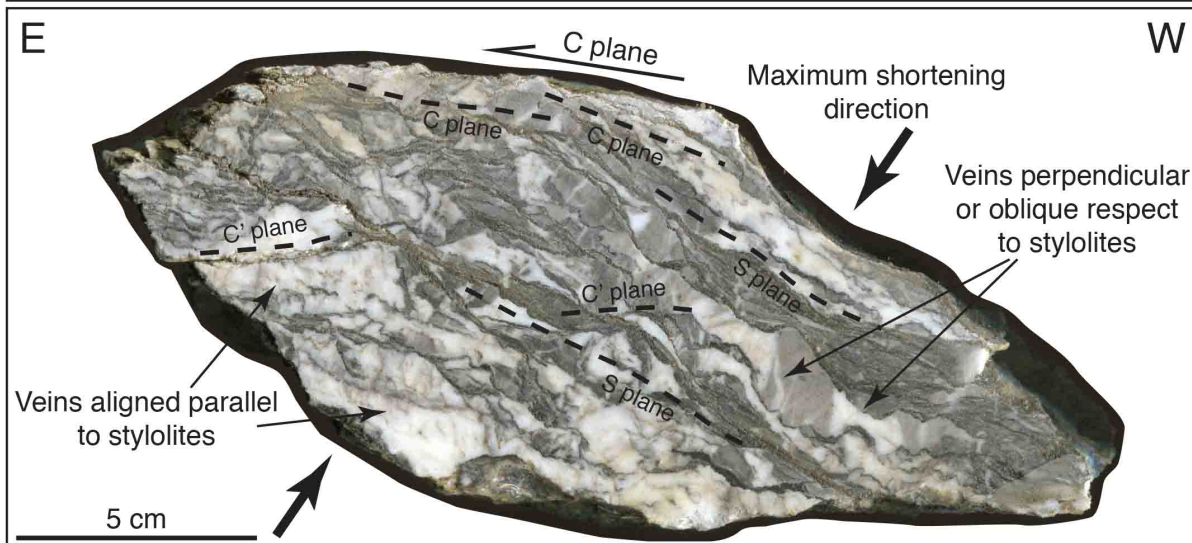
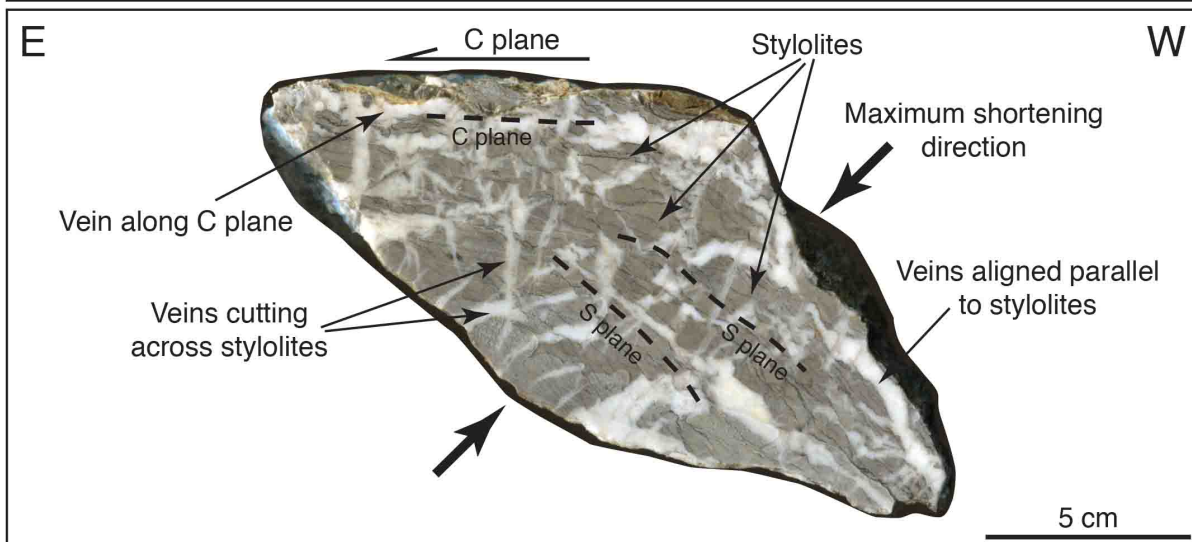
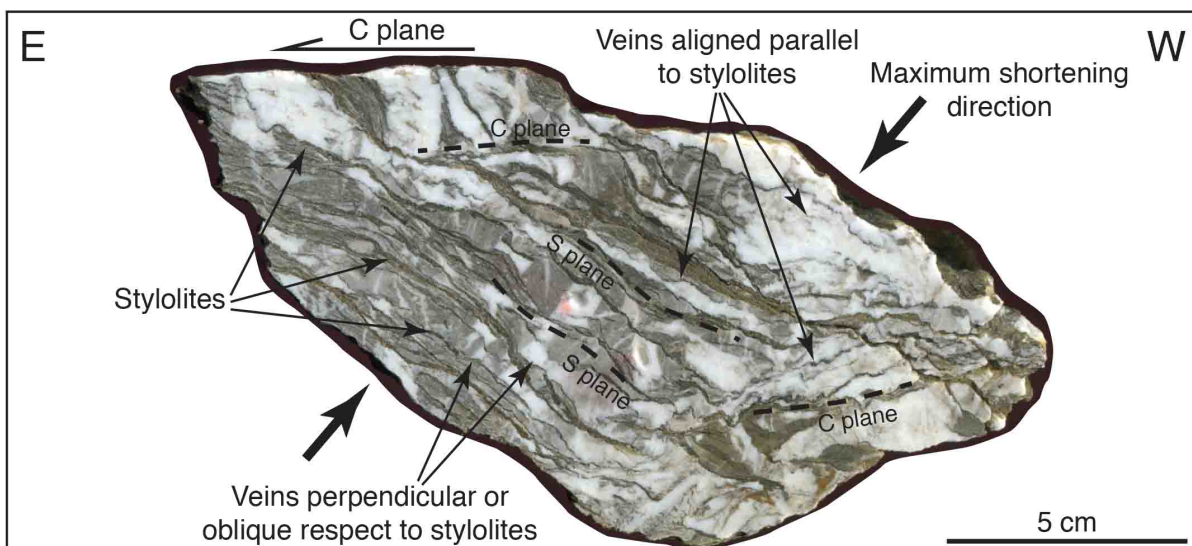




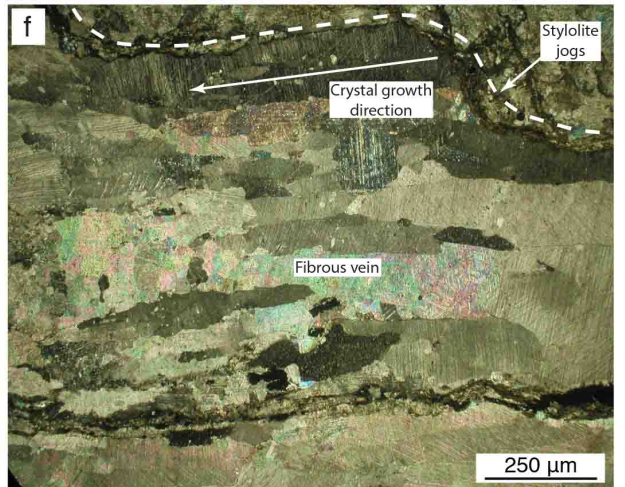
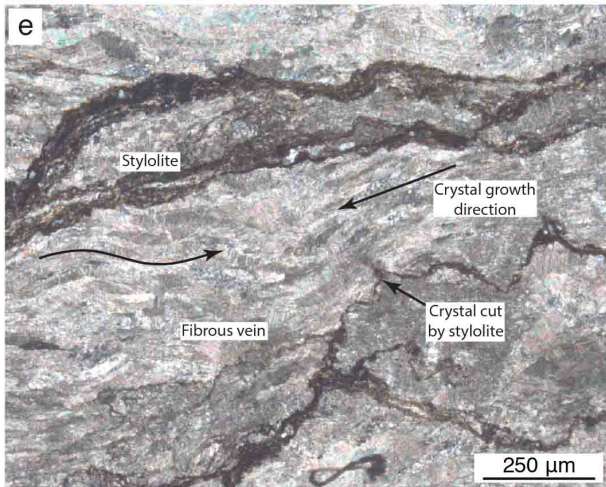
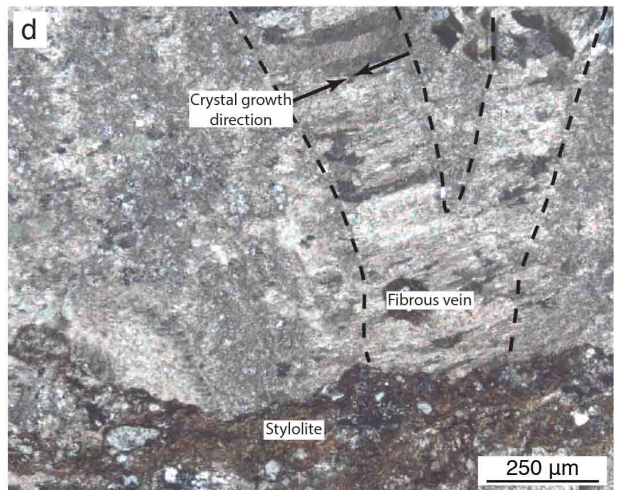
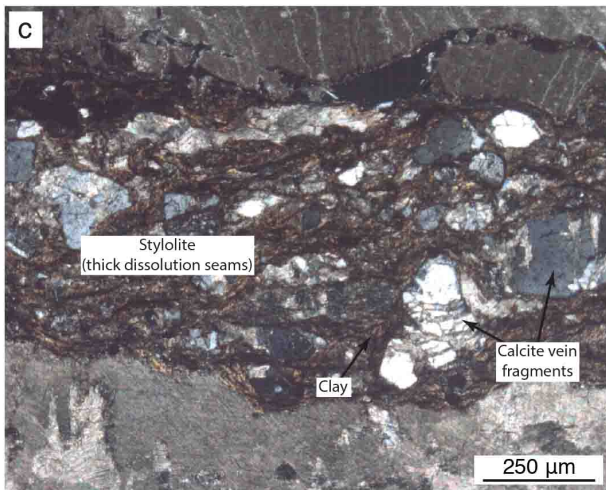
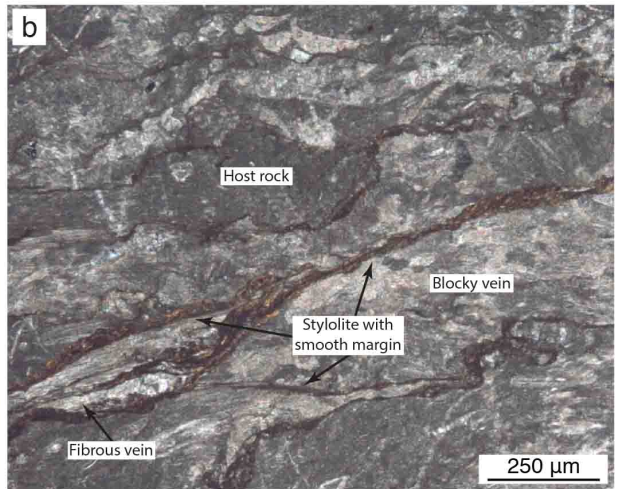
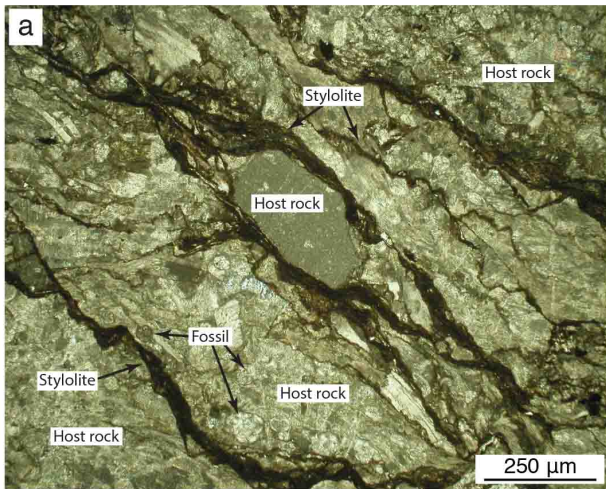




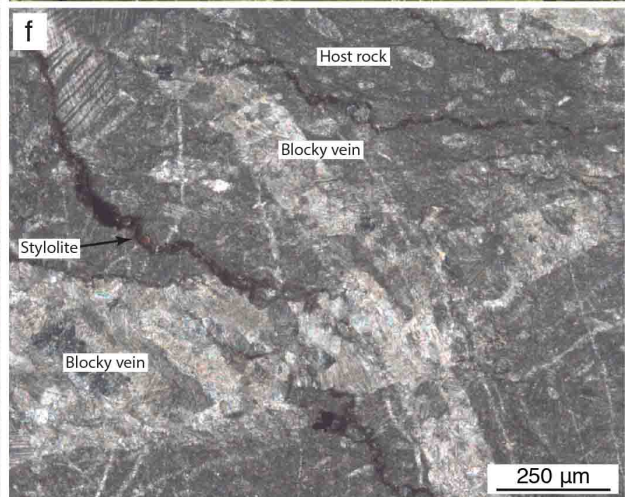
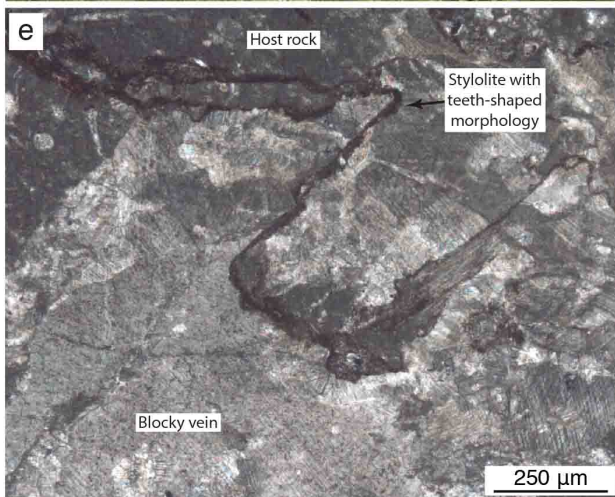
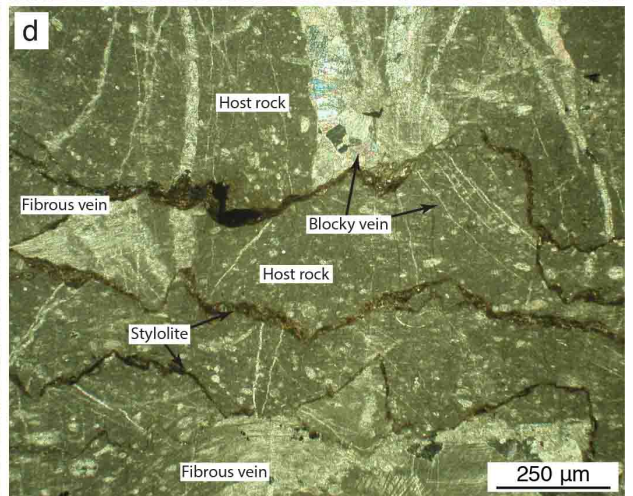
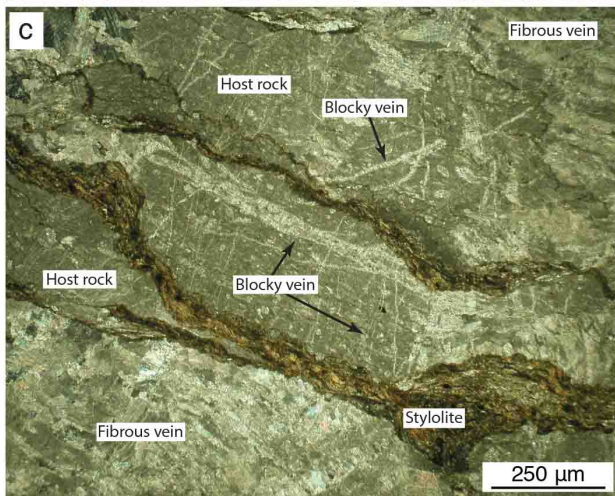
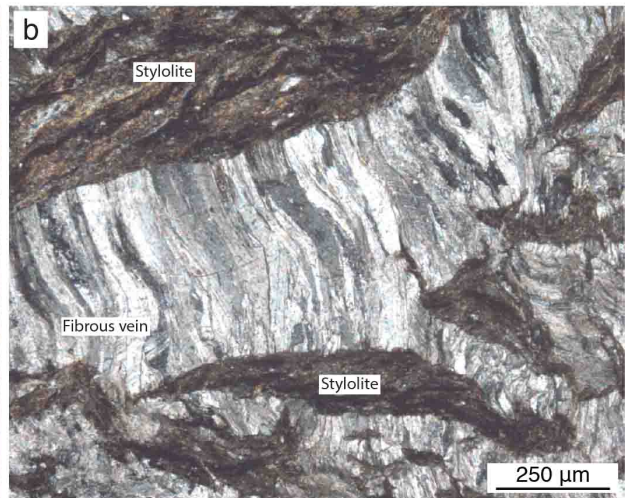
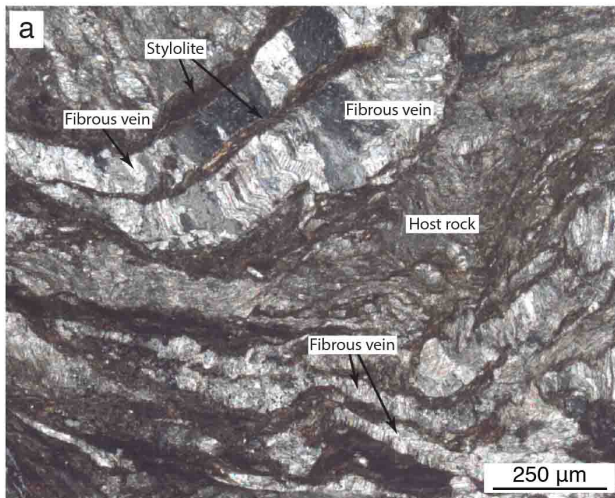
## Relicts of competent bedding



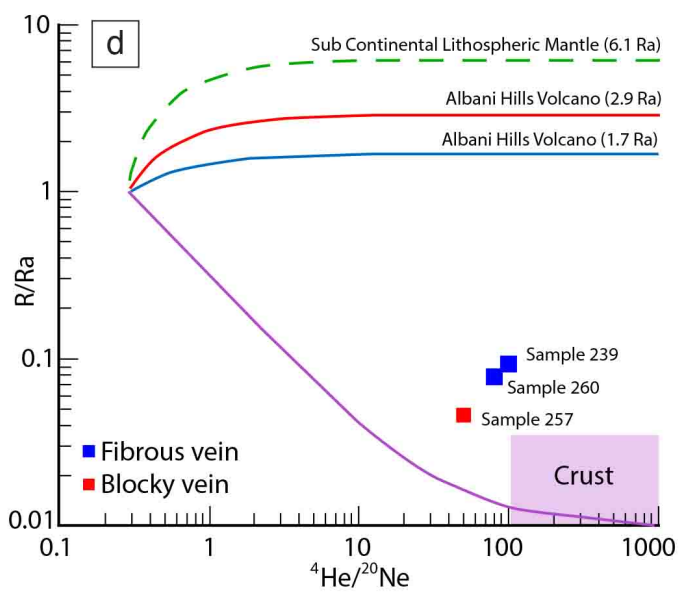
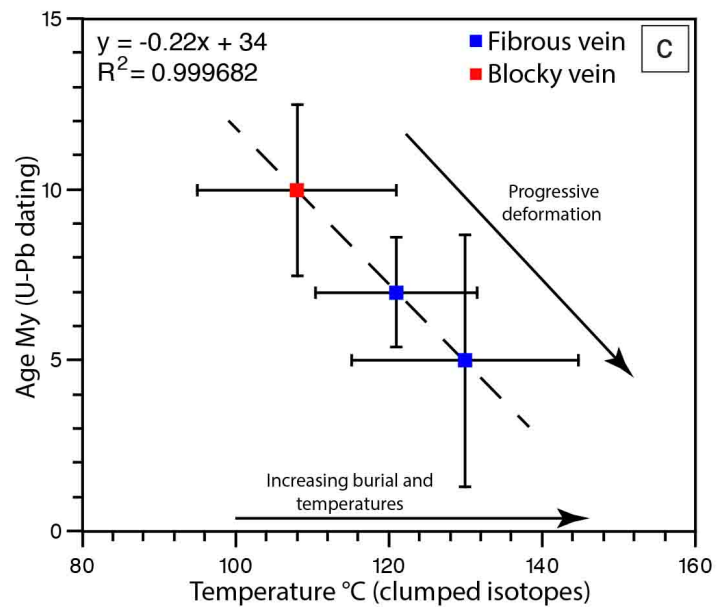
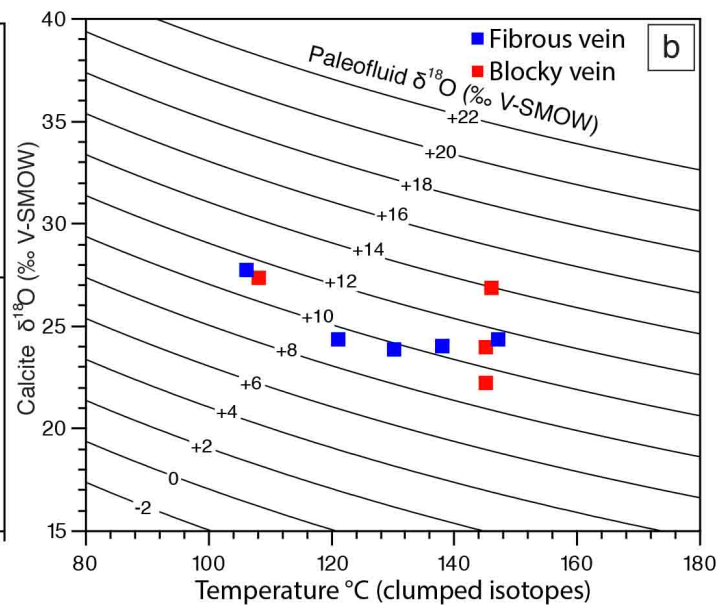
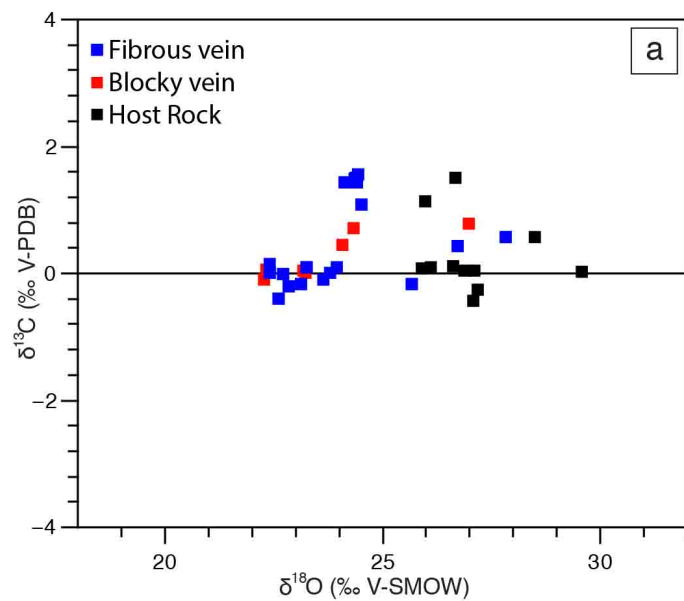


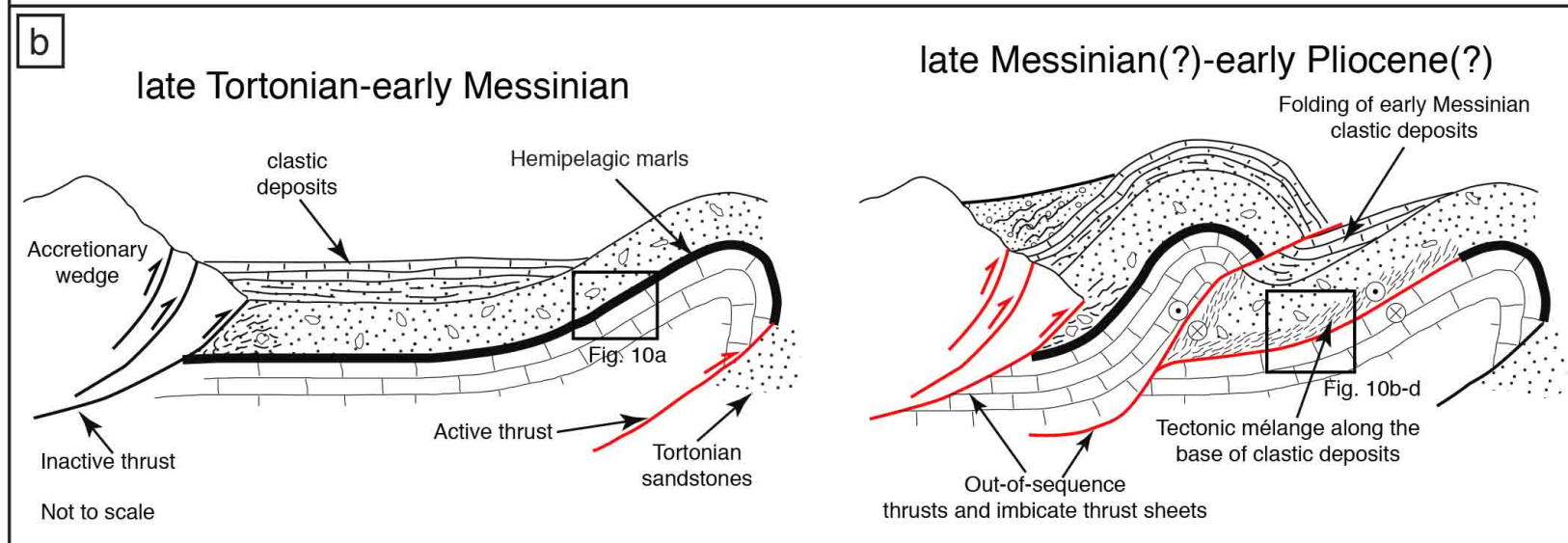
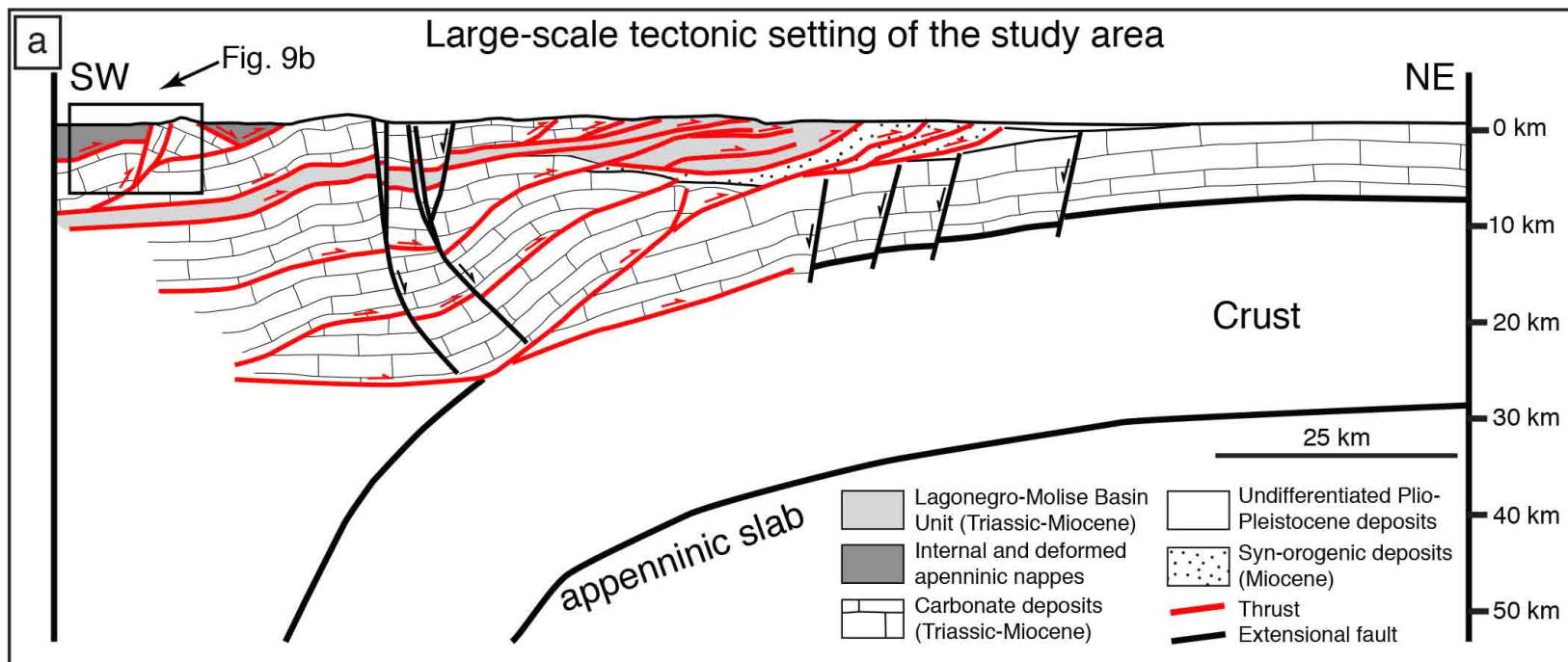




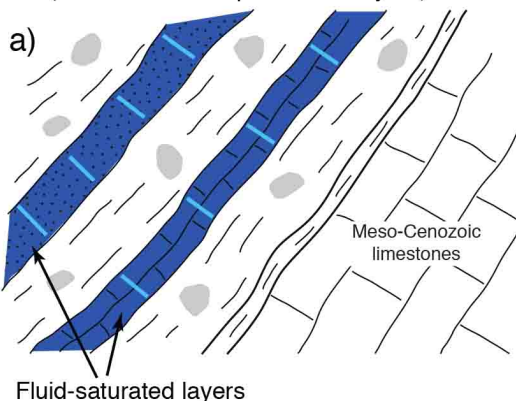




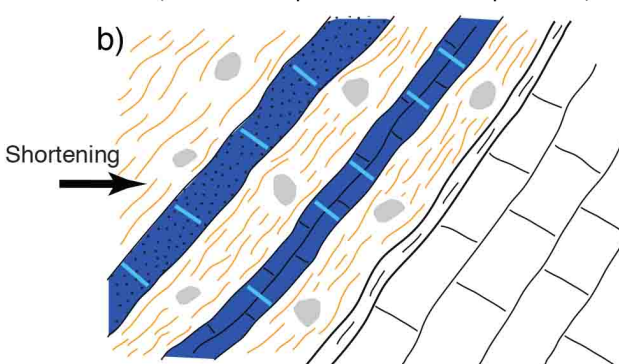




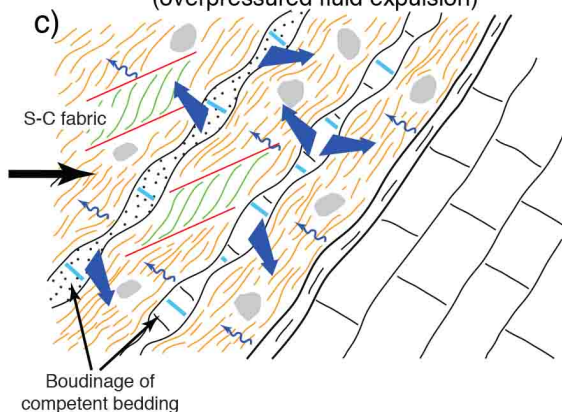
Early deformation stage  
(retained fluids in permeable layers)



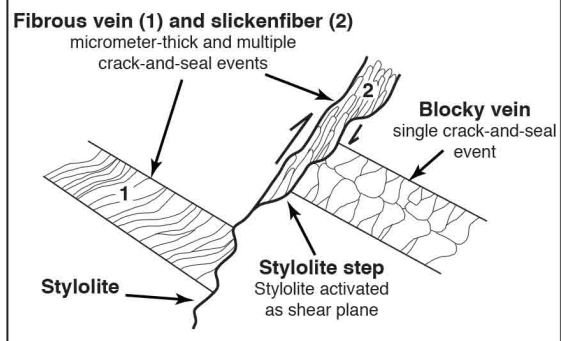
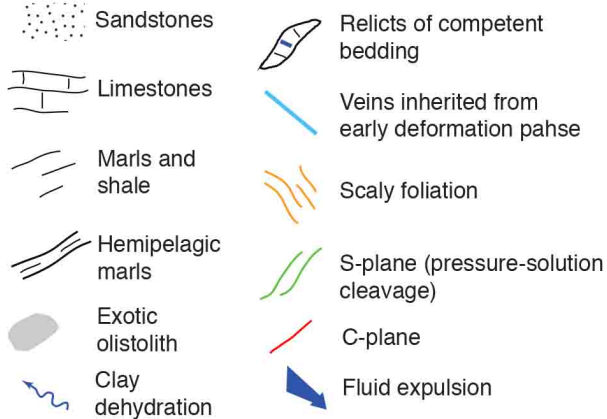
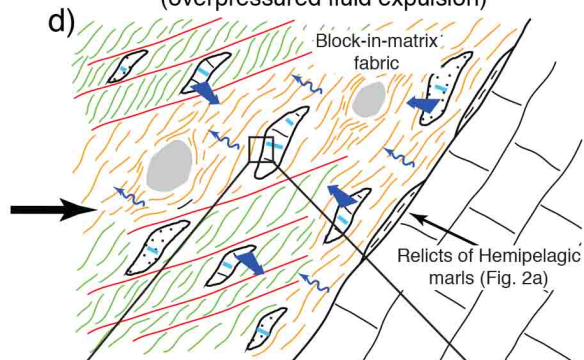
Poorly deformed clastic deposits  
(initial development of fluid overpressure)



Moderately deformed tectonic mélange  
(overpressured fluid expulsion)



Strongly deformed tectonic mélange  
(overpressured fluid expulsion)



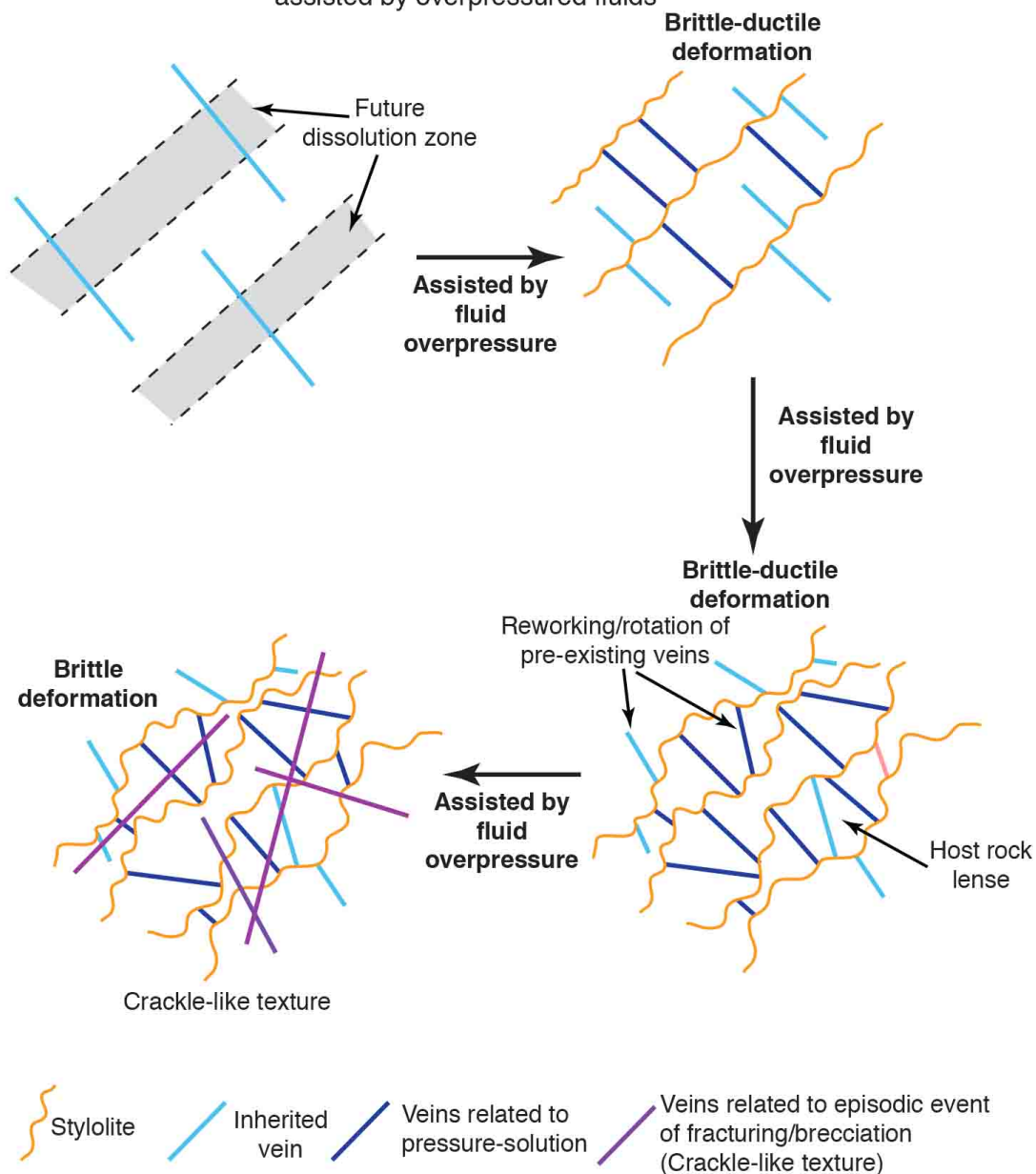


Strongly deformed tectonic mélangé (Fig. 10d  
(overpressured fluid expulsion)



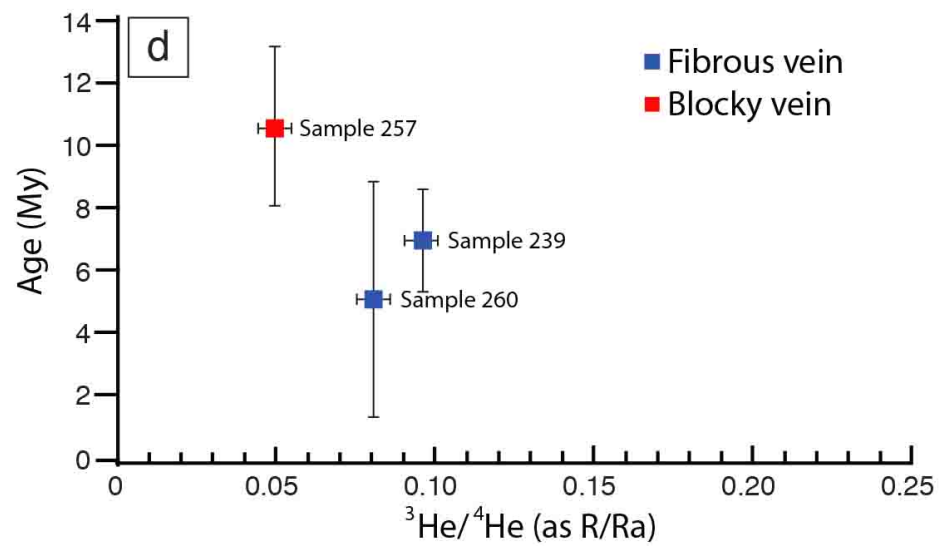
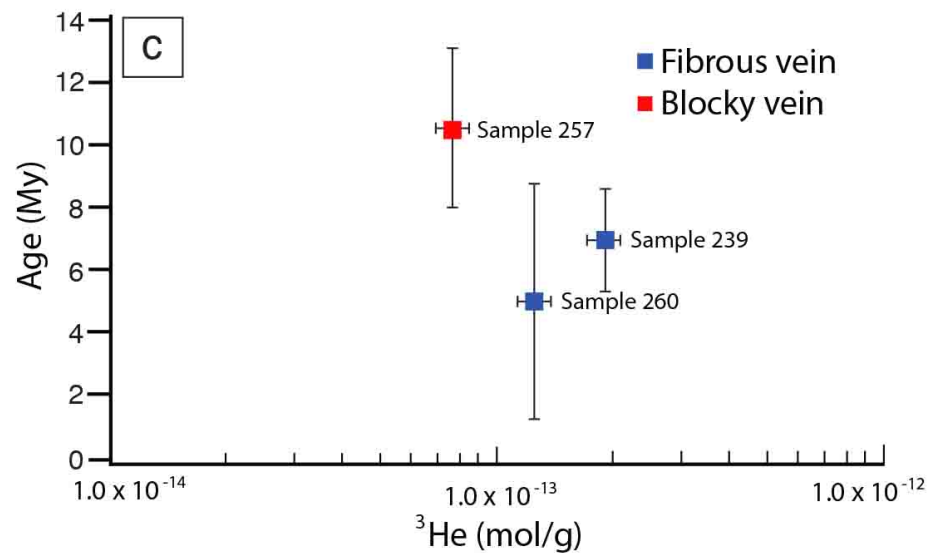
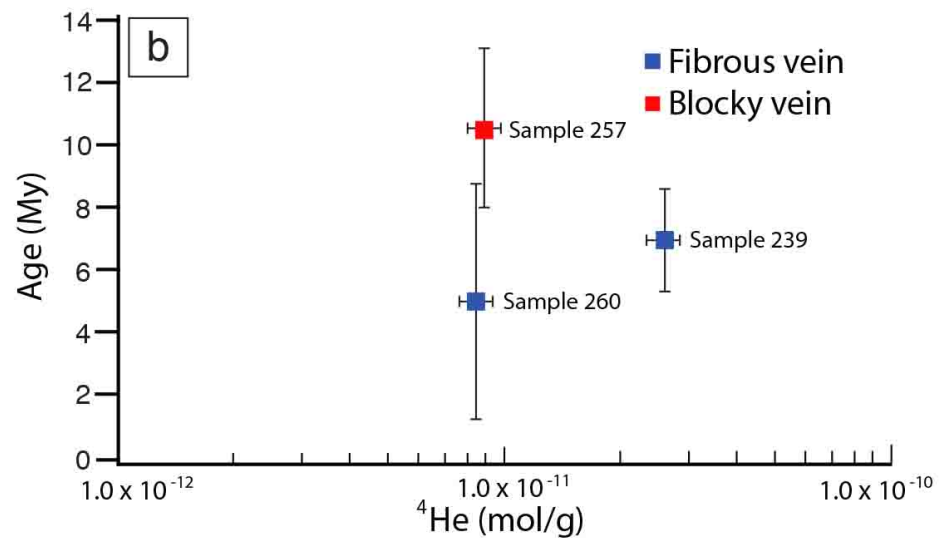
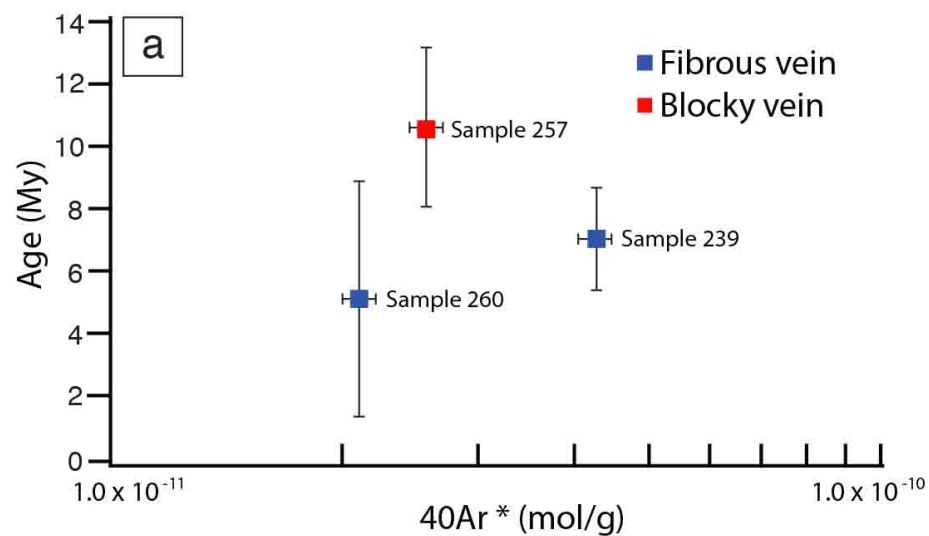
## Veins development within the tectonic mélangé

Cycles of mutually overprinting brittle and ductile processes  
assisted by overpressured fluids



**Declaration of interests**

The authors declare that they have no known competing financial interests or personal relationships that could have appeared to influence the work reported in this paper.



Locality	Number	Sample type	$\delta^{13}\text{C}$ ‰ (V-PDB)	$\delta^{18}\text{O}$ ‰ (V-SMOW)
N 41°09'59" E 13°53'03"	242	Blocky vein	0.45	24.05
N 41°09'59" E 13°53'03"	234	Blocky vein	0.73	24.31
N 41°09'59" E 13°53'03"	233-2	Blocky vein	0.80	26.97
N 41°09'59" E 13°53'03"	238-1	Fibrous vein	-0.38	22.61
N 41°09'59" E 13°53'03"	259	Fibrous vein	0.59	27.82
N 41°09'59" E 13°53'03"	235	Fibrous vein	0.44	26.70
N 41°09'59" E 13°53'03"	237-1	Fibrous vein	1.09	24.51
N 41°09'59" E 13°53'03"	237-2	Fibrous vein	1.56	24.42
N 41°09'59" E 13°53'03"	237-3	Fibrous vein	1.45	24.40
N 41°09'59" E 13°53'03"	237-4	Fibrous vein	1.50	24.35
N 41°09'59" E 13°53'03"	254-1	Fibrous vein	-0.09	23.62
N 41°09'59" E 13°53'03"	254-2	Fibrous vein	-0.16	25.65
N 41°09'59" E 13°53'03"	254-3	Fibrous vein	-0.19	22.84
N 41°09'59" E 13°53'03"	260-2	Fibrous vein	0.11	23.24
N 41°09'59" E 13°53'03"	260-3	Blocky vein	0.06	23.17
N 41°09'59" E 13°53'03"	260-4	Blocky vein	0.01	23.22
N 41°09'59" E 13°53'03"	260-5	Fibrous vein	0.11	23.94
N 41°09'59" E 13°53'03"	260-8	Fibrous vein	0.02	23.79
N 41°09'59" E 13°53'03"	265	Fibrous vein	0.16	22.40
N 41°09'59" E 13°53'03"	265-2	Fibrous vein	0.00	22.69
N 41°09'59" E 13°53'03"	265-3	Fibrous vein	0.01	22.40
N 41°09'59" E 13°53'03"	265-5	Blocky vein	-0.08	22.27
N 41°09'59" E 13°53'03"	265-6	Blocky vein	0.01	22.35
N 41°09'59" E 13°53'03"	265-7	Blocky vein	0.07	22.31
N 41°09'59" E 13°53'03"	266	Fibrous vein	1.44	24.11
N 41°09'59" E 13°53'03"	266 bis	Fibrous vein	-0.16	23.10
N 41°09'59" E 13°53'03"	266 S-plane	Fibrous vein	1.52	24.38
N 41°09'59" E 13°53'03"	HR 1	Host rock	0.58	28.48
N 41°09'59" E 13°53'03"	HR 2	Host rock	1.15	25.97
N 41°09'59" E 13°53'03"	HR 3	Host rock	0.04	29.56
N 41°09'59" E 13°53'03"	HR 4	Host rock	-0.42	27.06
N 41°09'59" E 13°53'03"	HR 5	Host rock	0.13	26.60
N 41°09'59" E 13°53'03"	HR 6	Host rock	0.05	27.10
N 41°09'59" E 13°53'03"	HR 7	Host rock	0.06	26.85
N 41°09'59" E 13°53'03"	HR 8	Host rock	0.09	25.89
N 41°09'59" E 13°53'03"	HR 9	Host rock	1.52	26.65
N 41°09'59" E 13°53'03"	HR 10	Host rock	-0.24	27.16
N 41°09'59" E 13°53'03"	HR 11	Host rock	0.11	26.08

**Table S1.** Summary of  $\delta^{18}\text{O}$ - and  $\delta^{13}\text{C}$ -isotopes analyses on mélange-related mineralizations

Sample type	Replicates	$\delta^{13}\text{C}$ V-PDB	$\delta^{13}\text{C}$ V-PDB SD	$\delta^{18}\text{O}$ V-PDB	$\delta^{18}\text{O}$ V-PDB SD	$\delta^{18}\text{O}$ V-SMOW	$\Delta 47$ CDES	$\Delta 47$ CDES SD	$\Delta 47$ CDES SE	Average T °C	SD	SE	68% Conf Level	95% Conf Level	$\delta^{18}\text{O}$ paleofluid (VSMOW) (O'Neil et al., 1969)
Blocky vein	10	0.78	0.01	-3.89	0.02	26.91	0.424	0.027	0.009	146	21.6	6.8	7.2	15.4	13.7
Blocky vein	11	0.44	0.02	-6.73	0.04	23.98	0.426	0.026	0.008	145	23.9	7.2	7.6	16.1	10.8
Blocky vein	8	0.67	0.02	-3.41	0.04	27.41	0.477	0.027	0.009	108	15.5	5.5	5.9	13.0	10.9
Blocky vein	13	0.02	0.11	-8.38	0.24	22.28	0.426	0.027	0.007	145	21.5	6.0	6.2	13.0	9.1
Fibrous vein	7	1.57	0.02	-6.32	0.03	24.41	0.424	0.026	0.010	147	22.3	8.4	9.1	20.6	11.3
Fibrous vein	10	0.06	0.02	-6.32	0.03	24.40	0.457	0.023	0.007	121	14.7	4.6	4.9	10.5	9.1
Fibrous vein	11	0.59	0.03	-3.04	0.06	27.79	0.482	0.034	0.010	106	20.4	6.2	6.4	13.7	11.0
Fibrous vein	8	0.10	0.01	-6.83	0.03	23.88	0.449	0.025	0.008	130	17.7	6.2	6.7	14.8	9.4
Fibrous vein	10	1.53	0.01	-6.64	0.02	24.08	0.433	0.015	0.005	138	11.0	3.5	3.7	7.9	10.3

**Table S2.** Summary of clumped isotopes analyses. SD, Standard Deviation; SE, Standard Error; CDES



Sample	Weight (g)	<sup>4</sup> He mol/g	<sup>4</sup> He err	<sup>3</sup> He mol/g	<sup>3</sup> He err	<sup>20</sup> Ne mol/g	<sup>20</sup> Ne err	H <sub>2</sub> O+CO <sub>2</sub> mol/g	N <sub>2</sub> mol/g	<sup>40</sup> Ar mol/g	<sup>40</sup> Ar err	<sup>40</sup> Ar* mol/g	<sup>40</sup> Ar* err	He/Ar	N <sub>2</sub> /Ar	He/Ne	He/Ar*	Err	R/Ra	Rc/Ra	Err tot +/-	<sup>40</sup> Ar/ <sup>36</sup> Ar	Error (%)
239	0,185	2,59 x 10 <sup>-11</sup>	0,02	3,38 x 10 <sup>-18</sup>	4,60	2,68 x 10 <sup>-13</sup>	0,65	8,28 x 10 <sup>-6</sup>	6,67 x 10 <sup>-7</sup>	1,84 x 10 <sup>-10</sup>	0,04	4,26 x 10 <sup>-11</sup>	0,08	1,41 x 10 <sup>-1</sup>	3633,289	96,5	0,61	0,1	0,10	0,09	0,004	388,88	0,07
260	0,112	8,42 x 10 <sup>-11</sup>	0,01	9,23 x 10 <sup>-19</sup>	5,76	1,06 x 10 <sup>-13</sup>	0,69	1,12 x 10 <sup>-6</sup>	3,07 x 10 <sup>-7</sup>	8,99 x 10 <sup>-11</sup>	0,07	2,10 x 10 <sup>-11</sup>	0,16	9,37 x 10 <sup>-2</sup>	3413,257	79,4	0,40	0,2	0,08	0,08	0,005	389,94	0,15
257	0,118	8,91 x 10 <sup>-11</sup>	0,01	6,04 x 10 <sup>-19</sup>	6,11	1,73 x 10 <sup>-13</sup>	0,61	2,58 x 10 <sup>-6</sup>	4,25 x 10 <sup>-7</sup>	1,38 x 10 <sup>-10</sup>	0,06	2,57 x 10 <sup>-11</sup>	0,13	6,48 x 10 <sup>-2</sup>	3092,841	51,7	0,35	0,1	0,05	0,05	0,003	367,29	0,12

**Table S3.** Summary of isotope data from fluid inclusions analysis of sin-tectonic calcite veins from the tectonic mélange

grain		<sup>207</sup> Pba	U	Pb	<u>Th</u>	<sup>206</sup> Pbd	±2s	<sup>207</sup> Pbd	±2s
		(cps)	(ppb)	(ppb)	U	<sup>238</sup> U	(%)	<sup>206</sup> Pb	(%)
A06	257	471600	1813	2050	1,45	0,6812	3,0	0,8316	0,29
A07		743113	2742	3190	1,59	0,6995	2,3	0,8354	0,26
A08		260035	1484	1140	1,75	0,4622	3,8	0,8341	0,36
A09		285988	1597	1222	1,33	0,461	3,8	0,8312	0,32
A10		337476	1242	1442	1,83	0,6985	3,7	0,833	0,31
A11		859984	2505	3710	1,34	0,8915	3,0	0,8333	0,26
A12		848268	2668	3655	1,04	0,825	2,4	0,8325	0,28
A13		848529	2950	3677	1,28	0,7508	2,8	0,8314	0,25
A14		178565	743	770	1,83	0,623	2,6	0,836	0,41
A15		289446	1019	1254	1,31	0,7413	2,9	0,8326	0,33
A16		600706	3321	2920	1,48	0,5291	12,8	0,8341	0,33
A17		39317	28	170	0,90	3,589	3,2	0,8401	0,83
A18		49523	41	216	0,27	3,142	4,4	0,8369	0,9
A19		26662	26	115	0,70	2,711	2,9	0,8369	1
A357	239	12788	285	65	0,02	0,1384	2,4	0,8223	1,2
A358		18181	191	96	0,02	0,303	2,8	0,8235	0,99
A359		14325	241	75	0,01	0,1893	2,6	0,8241	1,4
A360		10828	280	57	0,01	0,1228	2,4	0,8226	1,2
A361		10706	363	57	0,00	0,09543	2,5	0,8109	1,2
A362		10988	348	58	0,01	0,1019	2,9	0,8148	1,5
A363		12475	330	65	0,00	0,1201	2,2	0,8217	1,2
A364		17402	368	92	0,01	0,1525	2,6	0,8174	1,2
A365		15176	390	80	0,01	0,1241	2,2	0,824	1,4
A366		6761	174	36	0,04	0,1245	2,3	0,821	1,4
A367		8980	177	47	0,04	0,1606	2,6	0,8241	1,5
A368		4920	426	27	0,02	0,03843	2,7	0,8025	1,9
A369		4639	372	24	0,02	0,04009	2,9	0,8108	1,5
A370		5947	327	32	0,01	0,05904	2,5	0,8161	1,6
A371		9201	336	49	0,01	0,08899	2,3	0,8169	1,1
A372		9057	447	48	0,01	0,06531	2,2	0,8188	1,5
A373		6908	380	37	0,01	0,05856	2,6	0,8195	1,6
A374		7199	428	38	0,00	0,05435	2,4	0,8226	1,4
A375		5955	393	32	0,02	0,04907	2,7	0,813	1,5
A376		6757	314	36	0,02	0,06952	2,5	0,8158	1,7
A377		7776	396	42	0,01	0,06384	2,6	0,8122	1,6
A378		27871	67	148	0,09	1,339	2,3	0,8237	0,82
A379		36109	87	191	0,14	1,332	2,5	0,8282	0,66
A380		29563	77	157	0,08	1,237	2,5	0,827	0,79
A381		29869	62	155	0,08	1,511	2,2	0,8303	0,65
A382		6778	270	37	0,02	0,08265	2,7	0,816	1,4
A388		5744	357	31	0,02	0,05281	3,1	0,8086	1,7

A389		8213	359	44	0,01	0,07527	3,4	0,8178	1,3
A390		4465	466	24	0,00	0,03182	2,5	0,7943	1,6
A391		7002	296	38	0,00	0,07781	3,1	0,8133	1,9
A392		4777	310	26	0,01	0,05026	3,2	0,819	1,7
A393		4529	355	25	0,01	0,04272	2,6	0,8027	2,3
A394		5007	525	28	0,00	0,03264	2,6	0,7964	1,6
A395		6174	372	34	0,00	0,05504	2,5	0,8121	1,6
A396		6364	386	35	0,00	0,0553	2,4	0,8108	1,6
A397		7127	430	39	0,00	0,05461	2,3	0,8224	1,1
A398		6037	407	33	0,00	0,04976	2,6	0,8068	1,5
A279	260	13497	219	67	0,33	0,1848	5,4	0,8327	1,3
A280		5001	160	26	0,41	0,09853	3,6	0,8033	1,8
A281		5932	277	30	0,28	0,06634	4,0	0,8151	1,9
A282		4217	185	21	0,24	0,07005	3,4	0,8215	3
A288		2222	143	12	0,16	0,04938	4,1	0,7978	2,9
A289		2093	100	10	0,11	0,0627	3,5	0,8231	3
A290		4225	138	21	0,20	0,09378	3,8	0,8269	2,2
A291		2031	115	11	0,08	0,05615	3,3	0,8012	3,1
A292		3437	183	18	0,24	0,05916	2,6	0,8036	2,7
A293		2266	189	12	0,03	0,03706	3,3	0,8226	2,8
A294		2120	141	11	0,04	0,04753	4,1	0,8059	2,3
A295		2135	197	11	0,02	0,03456	2,8	0,7943	2,6
A296		3288	182	17	0,08	0,05596	4,8	0,8266	2,2
A297		1759	175	9	0,02	0,03171	3,6	0,8073	3,1
A298		1526	188	8	0,01	0,0265	3,3	0,7891	3,4
A299		1516	207	8	0,01	0,0253	3,2	0,7562	2,5
A300		2051	221	11	0,01	0,02958	4,8	0,7964	2,5
A301		3149	190	16	0,04	0,05305	3,5	0,7994	2,8
A302		3162	58	16	0,07	0,1711	2,6	0,8152	2,7
A303		5499	57	28	0,09	0,2944	2,9	0,8301	1,8
A304		1879	225	10	0,01	0,02713	3,2	0,7866	3,1
A305		2075	244	11	0,01	0,02725	3,9	0,7959	2,9
A306		3289	226	17	0,04	0,0464	4,5	0,8082	3,1
A307		1723	248	9	0,01	0,02306	3,2	0,7729	3,4
A308		2257	190	12	0,02	0,03743	3,2	0,813	3,2
A309		3923	20	20	1,77	0,602	3,9	0,8285	1,9
A310		3197	132	17	0,06	0,0771	4,4	0,809	2,7

**Table S4.** Summary of in situ U, Pb, and Th analyses of syn-tectonic calcite veins from the tectonic Mélange

## 1    **Methods**

### 3    **Stable and Clumped isotopes**

4        The stable and clumped isotope composition of the carbonates were determined at ETH  
5    Zürich using a Thermo Fisher Scientific MAT253 mass spectrometer coupled to a Kiel IV  
6    carbonate preparation device, following the method described in Schmid and Bernasconi (2010),  
7    Meckler et al. (2014), and Müller et al. (2017). The Kiel IV device included a PoraPakQ trap kept at  
8    -40°C to eliminate potential organic contaminants. Prior to each sample run, the pressure-dependent  
9    backgrounds were determined on all beams to correct for non-linearity effects in the mass  
10   spectrometer according to Bernasconi et al. (2013). During each run of the autosampler of 46  
11   positions, 3 replicates each of 95-110 µg of different samples and 5 replicates the carbonate  
12   standards ETH-1, ETH-2, and 10 replicates of the standard ETH-3 were analyzed with the LIDI  
13   method (Müller et al. 2017). The samples were measured over a period of three weeks to avoid  
14   biases due to short-term variations in the performance of the instruments. All calculations and  
15   corrections were done with the software Easotope (John and Bowen, 2016) using the revised  
16   IUPAC parameters for <sup>17</sup>O correction as suggested by Daeron et al. (2016). Temperatures were  
17   calculated using the O'Neal et al. (1969) calibration recalculated using fully recalculated values of  
18   the ETH standards and of calibration samples as described in Bernasconi et al. (2018). The  
19   complete results are reported in Table S3 in relation to the carbon dioxide equilibrium scale (CDES)  
20   projected to an acid digestion temperature of 25°C.

### 22   **Analytical technique for fluid inclusions**

23        We determined the H<sub>2</sub>O+CO<sub>2</sub>, and N<sub>2</sub> content and the elemental and isotope composition of  
24   noble gases (He, Ne, and Ar) in fluid inclusions of Sample 239, Sample 257, and Sample 260 of  
25   calcite veins from Mt. Massico tectonic mélange. Samples were prepared and analyzed in the  
26   laboratories of Istituto Nazionale di Geofisica e Vulcanologia (INGV), Sezione di Palermo (Italy),

27 following the preparation and analytical protocols described in Smeraglia et al. (2018) and Rizzo et  
28 al. (2019). Complete results are reported in Figs. 8d, S2 and Table S3.

29  $\text{H}_2\text{O}+\text{CO}_2$  in fluid inclusions have been extracted and quantified in a stainless steel crusher  
30 during noble gas extraction, which gives a good indication of the moles of gaseous matrix of fluid  
31 inclusions but does not completely preserve these species from adsorption and fractionation in  
32 powders and stainless steel. In the first stage, part of the vein samples has been gently broken,  
33 sieved with a diameter  $>1$  mm mesh. The selected crystals were cleaned in an ultrasonic bath. The  
34 portion of the selected sample material was weighed in an analytical balance, thus loaded into a  
35 stainless-steel crusher baked for 48-72h at  $120^\circ\text{C}$  in order to put in ultra-high-vacuum conditions  
36 ( $10^{-9}$  mbar). Fluid inclusions were released by a single-step (in-vacuum) crushing performed at  
37 200 bar. The amount of material loaded for each analysis was  $\sim 0.1$ - $0.2$  g. This procedure is the most  
38 conservative in order to minimize the contribution of cosmogenic  $^3\text{He}$  and radiogenic  $^4\text{He}$  possibly  
39 grown/trapped in the crystal lattice (e.g., Hilton et al., 1993, 2002). The atmospheric component  
40 was separated and quantified at the time of crushing by observing the following steps: immediately  
41 after crushing, we read the total gas pressure ( $\text{N}_2+\text{O}_2+\text{H}_2\text{O}+\text{CO}_2$ +noble gases). Then,  $\text{N}_2+\text{O}_2$ +noble  
42 gases were separated from the  $\text{H}_2\text{O}+\text{CO}_2$  by using a “cold finger” immersed in liquid nitrogen ( $T = -$   
43  $196^\circ\text{C}$ ) that allows freezing  $\text{H}_2\text{O}$  and  $\text{CO}_2$ . After this step, we checked again the total pressure for  
44 quantifying the atmospheric component. Noble gases separated from  $\text{H}_2\text{O}$  and  $\text{CO}_2$  were further  
45 cleaned in an ultra-high vacuum ( $10^{-9}$  -  $10^{-10}$  mbar) purification line, and all the species of the gas  
46 mixture, except noble gases, were removed from four getters.

47 Helium ( $^3\text{He}$  and  $^4\text{He}$ ) and neon ( $^{20}\text{Ne}$ ,  $^{21}\text{Ne}$  and  $^{22}\text{Ne}$ ) isotopes were measured separately by  
48 two different split-flight-tube mass spectrometers (Helix SFT-Thermo). The values of the  $^3\text{He}/^4\text{He}$   
49 ratio are expressed as  $R/R_a$  (where  $R_a$  is the  $^3\text{He}/^4\text{He}$  ratio of air, which is equal to  $1.39 \times 10^{-6}$ ). In  
50 addition, due to the presence of air He contamination, the  $R/R_a$  values were corrected based on the  
51 measured  $^4\text{He}/^{20}\text{Ne}$  ratio (e.g., Sano et al., 1985) and are expressed as  $R_c/R_a$  values. However, the

corrected ratios show minimum to negligible differences respect to raw  $^3\text{He}/^4\text{He}$  ratios. The analytical uncertainty of He isotopic ratio is  $\leq 6\%$ , while that of  $^{20}\text{Ne}/^{22}\text{Ne}$  is  $<0.17\%$ .

Argon isotopes ( $^{36}\text{Ar}$ ,  $^{38}\text{Ar}$  and  $^{40}\text{Ar}$ ) were analyzed by a multicollector mass spectrometer (GVI Argus), with an analytical uncertainty  $< 0.14\%$ . The uncertainty in the determinations of He, Ne, and Ar elemental contents was less than  $0.1\%$ . Typical blanks for He, Ne and Ar were  $<10^{-15}$ ,  $<10^{-15}$  and  $<10^{-14}$  mol, respectively, and are at least two orders of magnitude lower than analytical signals of samples. Further details about the sample preparation and analytical procedures are available in Rizzo et al. (2018, 2019) and Smeraglia et al. (2018).

60

## 61 References

- 62 Bernasconi S.M., Müller I. A., Bergmann K.D., Breitenbach S. F. M., Fernandez, A., Hodell D. A.,  
63 Jaggi M., Meckler A.N. Millan I., and Ziegler M. (2018) Reducing uncertainties in carbonate  
64 clumped isotope analysis through consistent carbonate-based standardization. *Geochemistry*  
65 *Geophysics Geosystems* 19. <https://doi.org/10.1029/2017GC007385>
- 66 Bernasconi, S.M., Hu, B., Wacker, U., Fiebig, J., Breitenbach, S.F.M., Rutz, T., 2013. Background  
67 effects on Faraday collectors in gas-source mass spectrometry and implications for clumped  
68 isotope measurements. *Rapid Communications in Mass Spectrometry*, 27, 603–612.  
69 doi:10.1002/rcm.6490
- 70 Breitenbach S.F.M, Mlenek-Vautravers, M.J., Grauel A.L., Bernasconi S.M. Müller, I.A., Rolfe, J.  
71 Gázquez F., Greaves M. Elderfield, H. and Hodell, D.A. (in revision) Coupled Mg/Ca and  
72 clumped isotope analyses of foraminifera provide consistent water temperatures. *Geochimica*  
73 *Cosmochimica Acta*.
- 74 Dennis, K.J., Affek, H.P., Passey, B.H., Schrag, D.P., Eiler, J.M., 2011. Defining an absolute  
75 reference frame for “clumped” isotope studies of  $\text{CO}_2$ . *Geochimimica et Cosmochimica Acta*,  
76 75, 7117–7131. doi:10.1016/j.gca.2011.09.025.

77 Hilton, D.R., Fischer, T.P., Marty, B., 2002. Noble gases and volatile recycling at subduction zones.  
 78 Rev. Min. and Geoch. 47, 319-370. <https://doi.org/10.2138/rmg.2002.47.9>.  
 79 Hilton, D.R., Hammerschmidt, K., Teufel, S., Friedrichsen, H. 1993. Helium isotope characteristics  
 80 of Andean geothermal fluids and lavas. Earth Planet. Sci. Lett. 120, 265-282.  
 81 [https://doi.org/10.1016/0012-821X\(93\)90244-4](https://doi.org/10.1016/0012-821X(93)90244-4).  
 82 John, C.M., Bowen, D., 2016. Community software for challenging isotope analysis: First  
 83 applications of “Easotope” to clumped isotopes. *Rapid Communications in Mass*  
 84 *Spectrometry*, 30, 2285–2300. doi:10.1002/rcm.7720  
 85 Kele, S., Breitenbach, S. F., Capezzuoli, E., Meckler, A. N., Ziegler, M., Millan, I. M., Kluge, T.,  
 86 Deak, J., Hanselmann, K., John, C.M., Yan, H., Liu, Z., Bernasconi, S.M. (2015).  
 87 Temperature dependence of oxygen-and clumped isotope fractionation in carbonates: A study  
 88 of travertines and tufas in the 6–95 °C temperature range. *Geochimica et Cosmochimica Acta*  
 89 168, 172-192. <https://doi.org/10.1016/j.gca.2015.06.032>.  
 90 Meckler, A.N., Ziegler, M., Millán, M.I., Breitenbach, S.F.M., Bernasconi, S.M., 2014. Long-term  
 91 performance of the Kiel carbonate device with a new correction scheme for clumped isotope  
 92 measurements. *Rapid Comm. in Mass Spectrom.* 28, 1705-1715.  
 93 Müller, I.A., Fernandez, A., Radke, J., Dijk, J. Van, Bowen, D., Schwieters, J., Bernasconi, S.M.,  
 94 2017. Carbonate clumped isotope analyses with the long-integration dual-inlet ( LIDI )  
 95 workflow : scratching at the lower sample weight boundaries. *Rapid Communications in Mass*  
 96 *Spectrometry*, 2, 1057–1066. doi:10.1002/rcm.7878  
 97 O'Neil, J. R., Clayton, R. N., & Mayeda, T. K. (1969). Oxygen isotope fractionation in divalent  
 98 metal carbonates. *The Journal of Chemical Physics*, 51(12), 5547-5558.  
 99 Rizzo AL, Pelorosso B, Coltorti M, Ntaflos T, Bonadiman C, Matusiak-Malek M, Italiano F and  
 100 Bergonzoni G (2018) Geochemistry of Noble Gases and CO<sub>2</sub> in Fluid Inclusions From  
 101 Lithospheric Mantle Beneath Wilcza Góra (Lower Silesia, Southwest Poland). *Front. Earth*  
 102 *Sci.* 6:215. doi: 10.3389/feart.2018.00215

103 Rizzo, A. L., Uysal, I. T., Mutlu, H., Ünal-İmer, E., Dirik, K., Yüce, G., et al. (2019). Geochemistry  
104 of fluid inclusions in travertines from western and northern Turkey: Inferences on the role of  
105 active faults in fluids circulation. *Geochemistry, Geophysics, Geosystems*,  
106 20. <https://doi.org/10.1029/2019GC008453>

107 Sano, Y., Urabe, A., Wakita, H., Chiba, H., Sakai, H., 1985. Chemical and isotopic compositions of  
108 gases in geothermal fluids in Iceland. *Geoch. J.* 19, 135-148.  
109 <https://doi.org/10.2343/geochemj.19.135>.

110 Schmid, T.W., Bernasconi, S.M., 2010. An automated method for “clumped-isotope” measurements  
111 on small carbonate samples. *Rapid Communications in Mass Spectrometry* , 24, 1955–1963.  
112 [doi:10.1002/rcm.4598](https://doi.org/10.1002/rcm.4598).

113